Diffraction Imaging Based on Marchenko Equation

by

©Xingtong Yue

A thesis submitted to the School of Graduate Studies in partial fulfillment of the requirements for the degree of

Master of Science

Department of Earth Science (Geophysics)

Memorial University of Newfoundland

June 2020

St. John's Newfoundland

Abstract

Diffractions are the primary carriers of information about small scale subsurface heterogeneities, such as fractures, faults, karsts and unconformities. However, the several orders of magnitude difference in amplitude between reflections and diffractions make diffraction imaging difficult. Many strategies have been used during processing and migration, but only few studies ever consider the influence of the survey geometry on diffraction imaging. The reason that the acquisition system can be now taken into account is because of the development of Marchenko redatuming. Given the data excited and recorded on the surface, the Marchenko equation can be used to redatum the sources and receivers to any desired position in the subsurface, with only basic prior information about the subsurface velocity and density. This makes the idea of improving diffraction imaging by adapting the survey geometry possible.

This study investigates how the depth and the shape of receiver sets influence diffraction imaging. A set of forward modelling results show that different layouts of the geometry do enhance the diffraction imaging and suggest two preferred layouts, receivers located in the subsurface as a line and a semi-circle. Then the Marchenko method is summarized from the literature by theoretically deriving the 1D and 3D Marchenko equations and practically introducing the workflow of Green's function retrieval. In the final chapter, using data generated from the surface geometry, the Marchenko redatuming is used to move the sources and receivers to the favourable location chosen during the forward modelling. The amplified diffraction imaging results indicate that the whole process we propose in this thesis is feasible.

Summary

In oil and gas exploration, the detection of the small scale subsurface geological bodies, such as fractures and faults are vital in locating an optimal well that targets the location of untapped resources. Diffractions are the primary carriers of information of these objects. However, there is a big difference between the energy of the reflections, which come from larger objects and the diffractions, resulting in difficulties in diffraction imaging. This thesis improves the diffraction imaging results by changing the source/receiver position a method called the Marchenko redatumming method. This method allows us to compute new data as though we had collected it at locations in the subsurface, which is not usually possible.

This study conducts a series of modelling experiments to investigate the influence of the source/receiver layout on diffraction imaging, finding two preferred layouts. When the receivers are placed on a line but in the subsurface near the scatterer or on a semi-circle around the scatterer in the subsurface, the diffraction imaging results improves substantially. Given the seismic data excited and recorded on the surface, the Marchenko method can redatum the sources and receivers to any desired position in the subsurface. The successful diffraction imaging results indicate that the whole process we propose in this thesis is feasible.

Acknowledgements

Firstly, I want to show my greatest appreciation to my supervisor, **Dr. Alison Malcolm**, for both professionally and personally supporting me during my master study. The supervision in weekly individual meeting help me make successive progress. I learnt how to be a good researcher from her. I also appreciate my committee member **Dr. Colin G. Farquharson** for the teaching and the advise on my proposal and my thesis.

I am thankful to **Dr. Polina Zheglova** for the help during the forward modelling, **Dr. Ivan Vasconcelos**, **Dr. Angus Lomas**, **Dr. Andrew Curtis** and **Dr. Filippo Broggini** for the technique support in Marchenko redatuming, **Dr. Heru Rusmanugroho** and **Mr. Kamal Moravej** for the discussion and the advise on my research, **Mr. Meghdad Darijani** for the help while I am taking the courses.

Personally, I want to thank **Dr. Somayeh K. Tadavani** for the accompany in my daily life, **Dr. Shangyu Du** for the critical ideas and encouragement during my thesis writing and **my parents** for the invaluable love.

Table of Contents

List of Figures

Chapter 1

Introduction

In spite of the size of many rock formation of interest, there are a number of the small scale subsurface features, such as fractures, faults, karsts and pinch-outs in underground that are also of interest. These small elements often affect oil and gas production, making the delineation of them important. In seismology, the response caused by these features is called a diffraction. In this Chapter we introduce the development of the diffraction imaging and the Marchenko method we use in this thesis.

1.1 Motivation

Physically, when the aperture of an obstacle is smaller than the wavelength, diffraction phenomena, the change in the direction of waves as they pass around an obstacle in their path, dominate the recorded signals (Liu, 2011). At the seismic scale, when a seismic wave hits these small scale subsurface heterogeneities, such as fractures, faults, karsts, pinch-outs and unconformities, diffracted waves are generated. The diffracted energy is the primary carrier of the information about these small subsurface elements (Neidell, 1997). A successful interpretation of these delicate structures can significantly increase the accuracy of the subsurface velocity information improving high-resolution seismic imaging.

The difficulties in imaging these scatterers come mainly because of the differences in

amplitude between reflections and diffractions, which can reach several orders of magnitude. Meanwhile, the dynamic and the kinematic characteristics of diffractions and reflections are different. To illustrate this, Figure 1.1a shows a synthetic velocity model with three reflectors and one point scatterer (diffractor) denoted as a red dsot in the middle of the model. The velocity of the red layers, the blue layer and the point scatterer are 5 km/s, 4 km/s and 5 km/s, respectively. The yellow star and the green dots on the upper boundary are sources and receivers respectively. Figure 1.1b shows a time snapshot of the wavefield. The circular wavefront labeled diffraction has quite a low amplitude compared to the reflection. This demonstrates the amplitude difference of reflections and diffractions. Figure 1.1c shows a shot gather containing both diffracted and reflected events, showing the subtle kinematic differences. Our goal in this thesis is to separate the diffraction from the total shot gather and subsequently get a high-quality diffraction image. We do this by recomputing new data with a different source/receiver geometry chosen to highlight the diffracted energy.

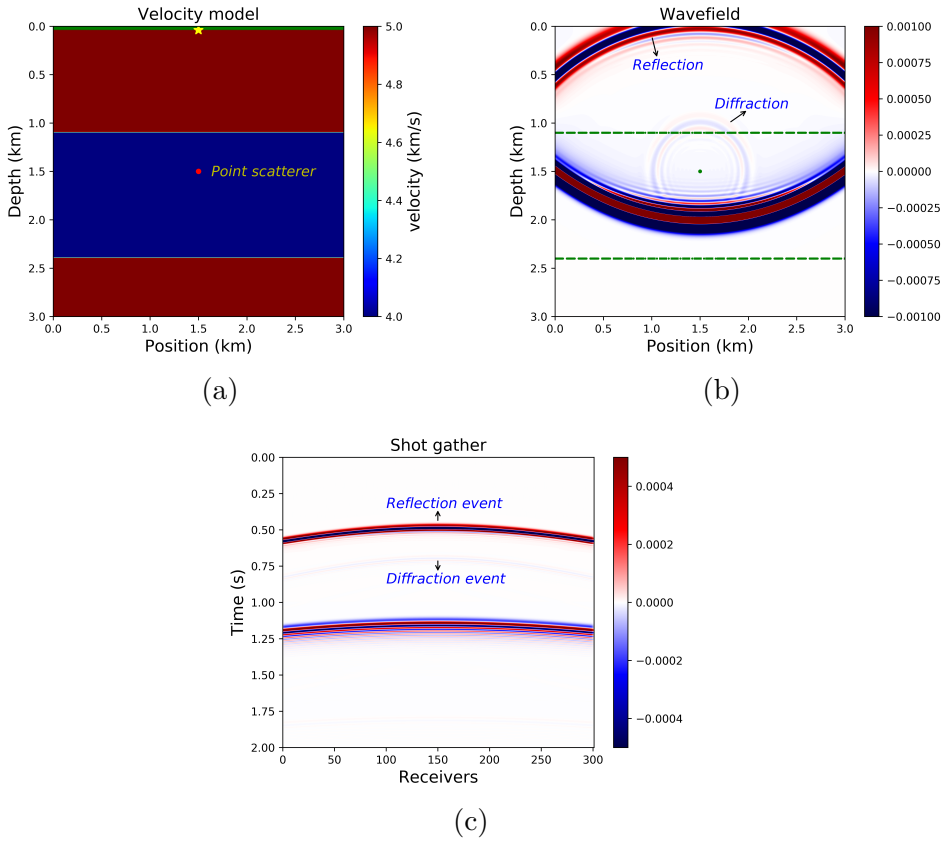

Figure 1.1: (a) Velocity model. (b) One snapshot of the wavefield. (c) Seismic shot gather.

Many efforts have been made to image diffractors, most of which can be organized into two categories. One of the mainstream methods of diffraction imaging is separating the diffraction and reflection data and conducting traditional migration on each separately. The other one is applying a filter, to filter out the specular energy during migration (Sturzu et al., 2014). But none of these methods consider that changing the source and receiver positions would make any difference to the diffraction imaging. Nowadays, a novel technique known as Marchenko Imaging has been widely used to reposition sources and receivers. This technique allows for the focusing of seismic data from the reflected data recorded at the surface to any preferred datum level in the subsurface. It is widely used in internal multiple removal (Meles et al., 2014), ghost-free imaging (Wapenaar et al., 2012), primary construction (Meles et al., 2015), source wavelet amplitude recovery (Mildner et al., 2017a) and velocity analysis (Mildner et al., 2017b). Our research shows that a well chosen source/receiver geometry

can significantly improve diffraction imaging (Chapter Two). Thus, we use the Marchenko technique to relocate the source and receivers to the preferred position to acheive better diffraction imaging.

1.2 Literature Review

1.2.1 Diffraction Imaging

The study of diffractions in seismology dates back to 1950s. Krey (1952) first clarified the importance of diffractions in carrying information of faults and fractures. Hagedoorn (1954) first took diffracted events into account when he conducted the initial migration attempt. Trorey (1970) contributes an early theoretical study of the behaviour of diffraction and Landa and Maximov (1980) prove the feasibility of separating scattered waves from strong specular reflections. Landa et al. (1987) calculate the signals along the diffracted travel time curve from common-offset sections and obtain a diffraction time image that shows the location of the diffractors. Kanasewich and Phadke (1988) modify Landa et al. (1987)'s method by using a common-fault-point section to take the diffracted energy into account. Tura et al. (1992) apply diffraction tomography techniques to field data and successfully detect fractures with their method.

In the late eighties and nineties, geophysicists focused on the application of diffracted information to characterize fractures. In the last two decades, the main interest turned to the separation of the diffracted and reflected wavefields. Khaidukov et al. (2004) separate reflected and diffracted wave fields by muting the reflected waves after focusing them to their imaginary source points, which are mirrored points on the opposite side of the reflector from the source. After muting this strongly focused reflected energy, defocusing the residual energy subsequently provides diffraction shot gathers, which can then be used to image the diffractions. Moser and Howard (2008) propose two techniques for diffraction imaging in depth. These two methods represent the two most popular categories of methods of diffraction imaging, mentioned above. The first category is separating the reflected and diffracted data and using traditional migration for each of them. The second category is applying a filter inside the migration kernel. In these techniques, a proper weighting function, which suppresses the specular energy, is added during the migration process, leading to a diffracted

migrated result. Taner et al. (2006) indicate that when they activate a plane wave source instead of a point source, the reflectors generate plane waves which appear on the seismic section as lines, while the diffractions still appear as hyperbolas. They call this the simulated plane wave section method, and follow it with a plane-wave destruction filter to suppress the reflected energy and produce diffraction sections. Berkovitch et al. (2009) propose a strategy named diffraction multifocusing stack (DMFS) based on multifocusing moveout corrections, which can precisely calculate the moveout of the diffractions. The optimal summation of the diffraction events will subsequently produce a section where diffractions are enhanced to the same amplitude level reflections, thus reflectors and diffractors can be migrated simultaneously. Klokov and Fomel (2012) conduct common-reflection angle migration in the dip-angle domain. The migrated data consists of a concave shaped reflection and a flat diffraction, which can be separated in the Radon domain. Sturzu et al. (2013) introduce a methodology called specularity gathers, which can efficiently construct a weight factor while migrating the data. This factor attenuates the reflection events which satisfy Snell's law, while preserving the diffracted events that do not. Sturzu et al. (2014) use the specularity gathers introduced by Sturzu et al. (2013) as a constraint to supervise the selection of the parameters of the specularity filter proposed in Moser and Howard (2008). The efficiency of this scheme is further proved by Sturzu et al. (2015). They show several field data examples in which the structural details that were masked under the reflected energy are revealed. The copious methodologies mentioned above show the efforts that researchers make to use different kinds of source (Taner et al., 2006), various domain and filters (Klokov and Fomel, 2012; Moser and Howard, 2008), diverse seismic data forms (Sturzu et al., 2013) and different data processing methods (Khaidukov et al., 2004; Moser and Howard, 2008) to separate the diffraction energy, but none of these methods consider the influence of the position of the sources and receivers on diffraction imaging. In Chapter Two I am going to use several numerical models to further discuss this.

1.2.2 Marchenko Redatuming

The Marchenko equation is the basis of 1D inverse scattering in mathematical physics and has been widely used since 1955 (Marchenko, 1955). It reveals the relationship between the reflection response, which is measured on one side of a medium, and a focusing field inside the medium, which has connections with the scattering potential in that medium. Snieder (2015) presents a historical overview of the Marchenko equation, explaining why it took so long for it to be used in Geophysics. Meanwhile he highlights the contribution made by Rose (2001). Rose (2001) states that the solution obtained from the 1D Marchenko equation focuses at a specified position inside the medium even in the absence of explicit medium knowledge or installation of receivers at the focusing point.

Broggini et al. (2011) as well as Broggini and Snieder (2012) clarify the relationship between seismic interferometry and the Marchenko equation. Both of these techniques aim to perform the same task of retrieving the Green's functions between an arbitrary virtual source inside the medium and a receiver at the surface. In the 1D case, the Green's functions retrieved by seismic interferometry need two-sided illumination as well as a physical receiver inside the medium. However, the scheme proposed by Broggini and Snieder (2012) needs no physical receivers inside the medium and one-sided illumination suffices. In addition, the Green's functions retrieved from seismic interferometry do not fully consider internal multiples, while those retrieved from the Marchenko equation do. This method is therefore also described as "beyond seismic interferometry".

Although the 3D form of the Marchenko equation, which is known as Newton-Marchenko (NM) equation, was already extended from 1D by Newton (1982), solving it requires omnidirectional reflection and transmission measurements, which are not available in seismic surveys. Wapenaar et al. (2013) combine the 1D approach of Broggini and Snieder (2012) with the reciprocity theorems for one-way wavefields (Wapenaar and Grimbergen, 1996) and derive a three-dimensional single-sided Marchenko equation which relates the single-sided reflection response of a 3D inhomogeneous medium to the field inside the medium. This

paper also shows how an iterative solution method for the single-sided 3D Marchenko equation leads to the 3D Green's function (including all multiple scattering). While dealing with Green's function retrieval issues, van der Neut et al. (2015) present an alternative technique, the coupled Marchenko equations, to achieve the same goal by iterative substitution.

Wapenaar et al. (2012) use "data-driven wave-field reconstruction" to obtain the correct up- and downgoing wave-fields. They claim that using these wave fields could lead to ghost-free imaging. Meles et al. (2014) present a new method to predict and remove internal multiples based on Marchenko redatuming and convolutional interferometry, using a relatively small number of virtual sources and no deconvolution. Similar to this method, Meles et al. (2015) proposes an alternative methodology to construct a dataset consisting of only primaries, which circumvents the need for both predicting and removing internal multiples. Singh et al. (2015) modify the earlier focusing algorithms (Wapenaar et al., 2013) to also take into account free-surface multiples. da Costa Filho et al. (2014) extend the theory and application of Marchenko imaging to elastodynamic media. Based on this method, da Costa Filho et al. (2015) then propose an elastic P- and S- autofocus imaging method that fully considers primaries and internal multiples caused by both the overburden and converted-waves. Meanwhile, current research has also developed the theory of Marchenko redatuming in complex media (Vasconcelos et al., 2015) and dissipative media (Slob, 2016). Ravasi et al. (2016) apply target oriented Marchenko imaging to real-field OBC data and generate encouraging imaging results of both shallow and deep structures. Additionally, in the comparison with a standard Reverse Time Migration (RTM) image, the Marchenko redatuming result reveals more continuous structures. Ravasi (2017) unites a one-way version of the Rayleigh integral representation with the coupled Marchenko equations to obtain a method they call Rayleigh-Marchenko redatuming which could soften the strict requirements on the input data when applying Marchenko redatuming to practical problems. Mildner et al. (2017b) build a target-oriented velocity model with Marchenko-redatumed data, which enables the correct updating of the velocity model, even if with an incorrect initial model. Mildner et al. (2017a)

subsequently demonstrate that using the focusing function f_1 could accurately recover the amplitude spectrum of the source wavelet. Lomas et al. (2019) use vertical seismic profile data as input to the Marchenko scheme and successfully image a vertical structure. Mildner et al. (2019) use the upgoing focusing function to perform the accurate wavelet estimation and in return lead to a higher quality Marchenko redatumed result. Brackenhoff et al. (2019) illustrate the Marchenko imaging work flow for synthetic and field data. They explain five limitations of the Marchenko method using field data. The results show that the Marchenko method is highly sensitive to the homogeneous media assumption, source and receiver spacing, minimum offset, aperture limitations and wavefield absorption. In this research, we find that the Marchenko method is also very sensitive to the wavelet, amplitude of the reflection response and the quality of the data. These will be discussed in more detail in Chapter Three.

1.3 Outline

The main body of my study is divided into three parts.

Chapter Two discusses the potential geometrical influences on diffraction imaging when the sources and receivers go beyond the limitation of being located on the traditional acquisition surface. Specifically, in this thesis, we place a point scatterer in our models to induce diffractions in the numerical forward modelling. In the first section, a number of simulations are conducted to test the best relative source-receiver locations in the subsurface if the receivers are located as a line. In the following section, I propose that if the receivers lay in semi-circles in the subsurface, using different filters can result in better diffraction results. In this Chapter, we use an existing finite-difference code to model the wave fields and write a Reverse time migration (RTM) code to do the diffraction imaging.

Chapter Three goes through the theoretical details of Marchenko equation and the workflow of conducting Marchenko imaging for the numerical data. In the first section, I summarize the derivation of the solution to the 1D Marchenko equation with an iterative strategy. In the second section, a widely used iterative solution to the 3D Marchenko equation is illustrated, which is the kernel of the redatuming algorithm used in Chapter 4. In the third section, I go through the specific steps of the Marchenko imaging procedure with a numerical model. This subsequently proves that relocating the sources and receivers to the subsurface leads to improved imaging results. In this Chapter, we use the Marchenko code and the seismic interferometry code to redatum the source/receivers and use the f-k filter to filter the reflection energies.

In **Chapter Four**, I apply the efficient Marchenko method illustrated in Chapter Three to a numerical model with a diffractor. With the help of the Marchenko redatuming, we relocate the source and receivers to our preferred location in the subsurface. Integrating the conclusions I draw in Chapter Two, I prove that using Marchenko redatuming can give a better diffraction imaging result.

In **Chapter Five** I discuss the results, as well as giving some conclusions and describing

some potential future directions.

Chapter 2

Influence of the Geometry on Diffraction Imaging

Moving the acquisition system into the subsurface will avoid the difficulty of removing the signature of the complex overburden, thus we hypothesize that changing the acquistion geometry to a geometry more favourable for recording diffractions will result in improved diffraction images. We consider the change of the geometries in two aspects, one is the depth of the sources and the receivers, the other is the shape of the layout of the receivers. In the first part, we locate the receivers conventionally on a straight line, but the depth of the sources and receivers changes. We identify four factors of the geometry locations that may affect the diffraction imaging, illustrated with forward modelling results. In the second part, considering of the amplitude characteristics of the diffracted waves, we locate the acquisition surfaces as semicircles and use an f-k filter to separate the diffracted data from the reflected data and this layout gives a improved diffraction image. In this chapter, we do not use the Marchenko method but exploit the flexibility of numerical modelling to place our sources and receivers in the subsurface.

2.1 Acquisition Surfaces Placed as Straight Lines

In this section, we are going to discuss how the vertical positions of the source and the receivers affect the diffraction imaging. We use the finite difference method to do the forward modelling and the RTM algorithm to do the imaging. Thus, while evaluating the effect of the source/receiver position on the diffraction imaging, the restrictions of the algorithms need to be considered. The lateral layout of the receivers is conventionally straight, but the depth of the source and receivers are flexible in the numerical modelling. While designing the different layout geometries, there are several factors that we take into consideration. We assume that moving the source/receivers closer to the point scatterers to avoid the upper layers will help to improve the diffraction imaging. We also test the imaging results of placing the sources and the receivers on different side of the point scatterer. A conclusion of how the depth of the geometry affects the diffraction imaging will be drawn at the end of this section.

2.1.1 Explanation of the Model

In this section, we explain the models and the data generated from them. Figure 2.1a is a velocity model with extent 3 km by 3 km, where the velocity of the blue and the red layers are 4 km/s and 5 km/s, respectively. The red dot in the third layer at depth 1.75 km is a point scatterer of 4.5 km/s velocity. The lateral and vertical spatial interval is 10 m. The time step is 0.33ms. The frequency of the source is 20 Hz. The yellow star is the source and the green triangles are the receivers. In our numerical modelling, we use three sources and 301 receivers, which are evenly distributed across the model. In the illustrations here, we only draw the middle source in the velocity models. Figure 2.1b is the shot gather generated from the model shown in Figure 2.1a when the source is in the middle. The data plotted in Figure 2.1b consist of the direct event, reflection events and diffraction events. The diffraction events are very weak and overwhelmed by the strong reflective events. Figure 2.1c is the RTM image migrated from the total shot gather 2.1b, but with three sources. The

layers are precisely located but the point scatterer cannot be seen. The energy differences between the reflections and the diffractions make the point scatterer image invisible under the amplitude scale in Figure 2.1c.

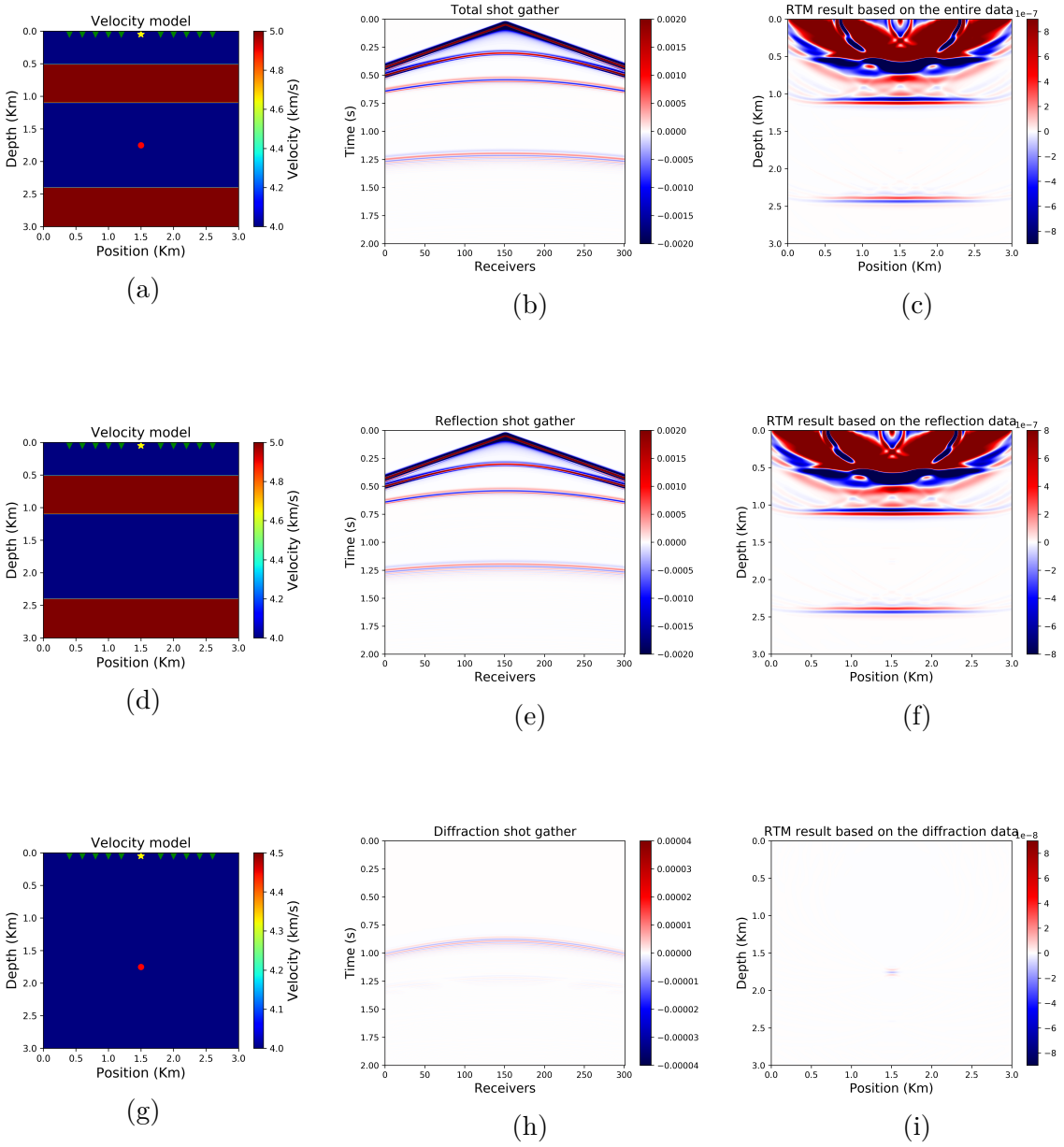

Figure 2.1: (a) Whole velocity model. (b) Total shot gather generated from velocity model (a). (c) The RTM result generated from the total shot gather (b) and two other shot positions. (d) Layered velocity model. (e) Reflection shot gather generated from velocity model (d). (f) RTM result generated from the reflective shot gather (e). (g) Diffractive velocity model. (f) Diffraction shot gather calculated by subtracting (e) from (b). (i) RTM result generated from the the diffraction shot gather (h).

Figure 2.1d is a layered model without the point scatterer inside. Figure 2.1e is the pure reflection shot gather generated from model 2.1d. Figure 2.1f is the RTM result based on the reflection shot gather.

Subtracting the reflection shot gather 2.1e from total shot gather 2.1b leads to the pure diffraction shot gather (Figure 2.1h). Notice that, the total shot gather (Figure 2.1b) and the reflection shot gather (Figure 2.1e) are plotted on the same amplitude range of [-0.002, 0.002], while the diffraction shot gather (Figure 2.1h) has a smaller range of [-0.00004, 0.00004] in order to reveal the diffraction events. The energy of the diffractions are always several magnitudes smaller than the reflections. Figure 2.1i is the RTM result calculated from the diffraction shot gather 2.1h. Using the same amplitude scale with the reflections, the point scatterer cannot be seen. For better understanding, shot gather 2.1h can be regarded as calculated by model 2.1g, which only contains a point scatterer in the homogeneous background.

In the later comparison, I will only show the whole velocity model (as in Figure 2.1a), the total shot gather (as in Figure 2.1b), the total RTM result (as in Figure 2.1c), the subtracted diffraction shot gather (as in Figure 2.1h) and the diffractive RTM result (as in Figure 2.1i). Notice that the amplitude range of the diffraction RTM result is shrunk to 0.1 times of that of the reflection RTM result in order to reveal the migrated point scatterer. The total RTM result is accessible from the field data so it is the standard of judging a geometry. The diffractive RTM images are ideal numerical modelling results, and are used as an auxiliary judging standard. The relative positions of the geometry to the point scatterer are tested, leading to four guiding tips to help locate the geometry in the subsurface, given in the final subsection.

In this thesis, all the shot gathers are calculated by finite difference method coded in C++ and displayed in Python. The RTM imaging is calculated using the RTM kernel provided by Pysit and displayed in Python.

2.1.2 Factor I: Distance Between the Geometry and the Point Scatterer

Figure 2.2 shows three layouts of the geometry. The first model (2.2a) contains the conventional geometry, located at the acquisition surface. Since the Marchenko redatuming helps us relocate the sources and receivers flexibly, we first try to move the receivers into the subsurface and close to our diffractive target (model 2.2b). In model 2.2b, the receivers are at depth 0.75 km. As the receivers get closer to the point scatterer, the energy of the events in the diffraction shot gather 2.2h are stronger than those in 2.2g. In addition, the point scatterer is just barely visible in the total RTM result (Figure 2.2k). Moving the receivers closer to the diffractions shortens the path that the diffracted waves need to travel, which preserves the diffracted energy and reduces the geometric divergence. Thus the closer the receivers are to the point scatterer, the stronger the diffraction image is.

Model 2.2c moves the source closer to the point scatterer at depth 0.75 km. The energies of the diffraction events in Figure 2.2i are even stronger compared with those in Figure 2.2h. The image of the point scatterer (pointed out by the black arrow) in Figure 2.2l also improves significantly. This is because there is less overburden for the signal to travel through, making the imaging problem easier.

From the results of these experiments, we conclude that decreasing the distance from the source or the receivers to the point scatterer will improve the diffraction imaging. Meanwhile, as the source/receivers approaching the point scatterer, the complex overburden is avoided and the energy loss due to reflection at the layer boundaries is saved.

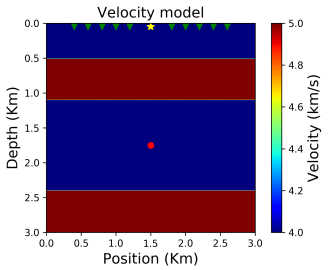

(a)

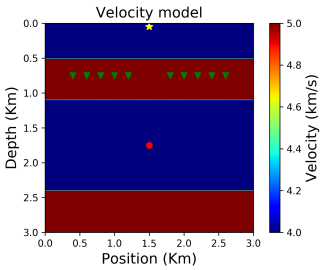

(b)

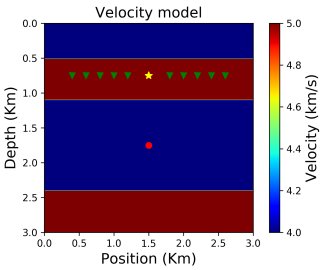

(c)

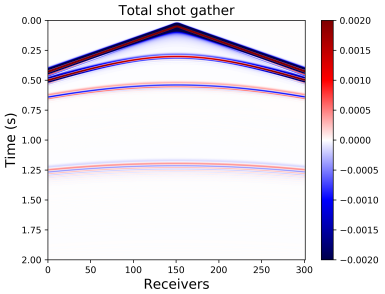

(d)

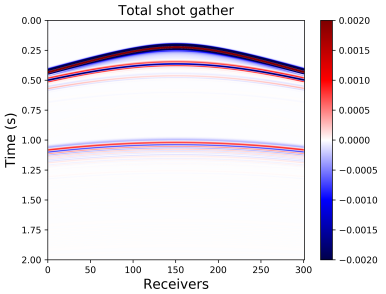

(e)

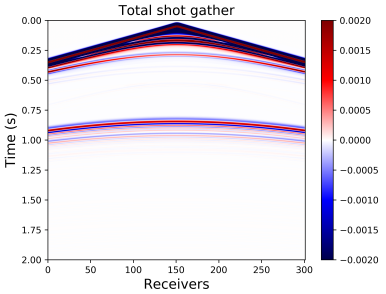

(f)

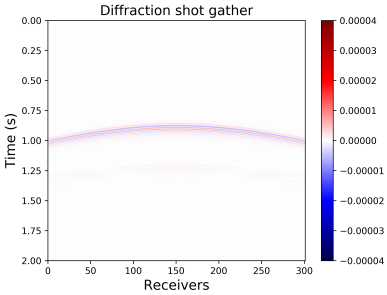

(g)

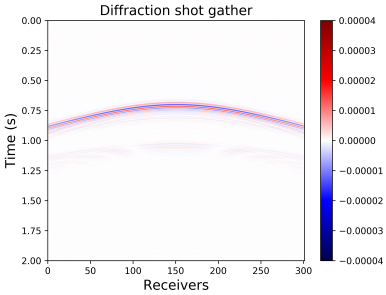

(h)

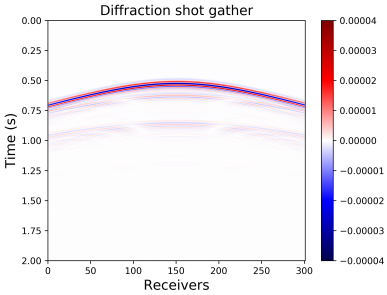

(i)

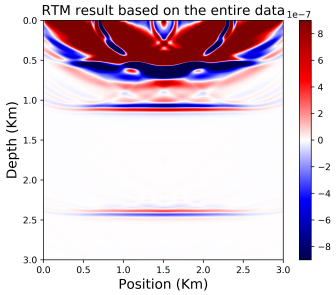

(j)

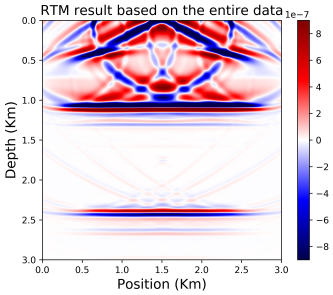

(k)

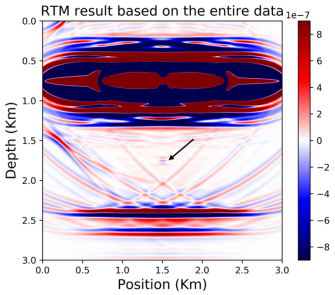

(l)

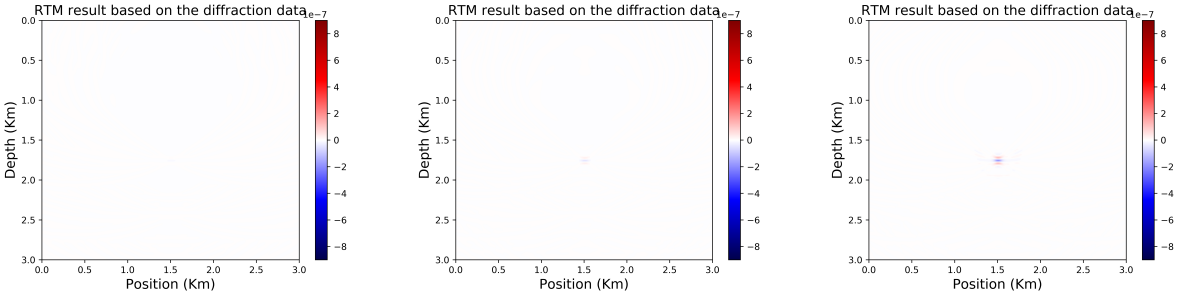

(m) (n) (o)

Figure 2.2: Three different layouts of the geometry in the same model and their corresponding seismic data and RTM imaging results. First row: Velocity models with different layouts of the geometries; Second row: Total shot gather generated from velocity model above; Third row: Diffraction shot gather; Fourth row: RTM results generated from the total shot gathers shown in the second row; Last row: RTM results generated from the diffraction shot gathers shown in the third row.

2.1.3 Factor II: Source Artifacts

In this section, we continue exploring moving the geometry closer to the point scatterer. At this point, model 2.3a is the best geometry we have so far, repeating that used in Figure 2.2c. Obeying the rule that the closer the geometry is to the point scatterer and the fewer interfaces that backscatter the energy the better the diffraction imaging is, we further move the sources and receivers closer to the scatterer point. In the model 2.3b, the geometry and the point scatterer are in the same layer at depth 1.4 km. From diffraction shot gather 2.3h we observe that the diffraction energy does get stronger, but the diffraction image in Figure 2.3k becomes strongly affected by source artifacts, which are brought in while doing RTM. Even the ideal diffractive RTM imaging (Figure 2.3n) from the pure diffraction shot gather (Figure 2.3h) shows the influence brought by source approaching the point scatterer. These artifacts could easily be mistaken for another diffractor in a more realistic example.

Figure 2.3c is a similar geometry with the source and receivers located at 2.15 km, showing that in a limited depth range, the imaging of the subsurface will be highly affected by the source artifacts, as shown in the red boxes in Figure 2.3n and 2.3o. We can avoid the artifacts by putting the geometry and the point scatterers in different layers like model 2.3a does. Thus, we need to update the conclusion we extracted at the end of Chapter 2.1.2, the geometry should be placed close to the target but while avoiding source artifacts at the same time, typically by keeping the geometry in a different layer than the point scatterer.

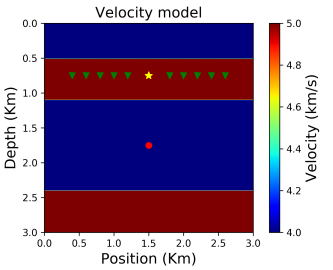

(a)

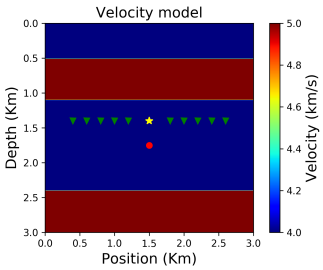

(b)

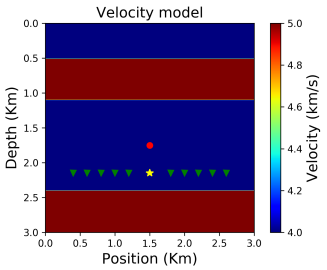

(c)

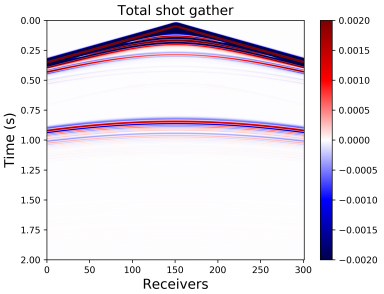

(d)

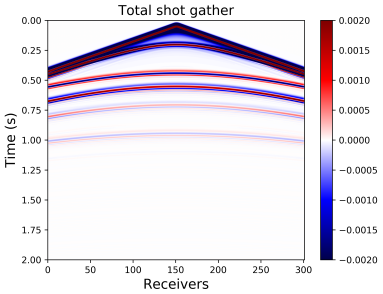

(e)

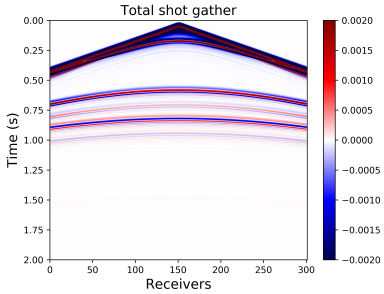

(f)

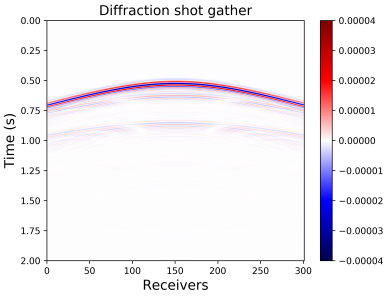

(g)

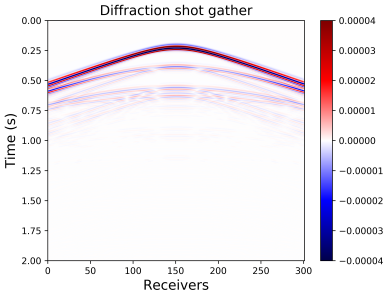

(h)

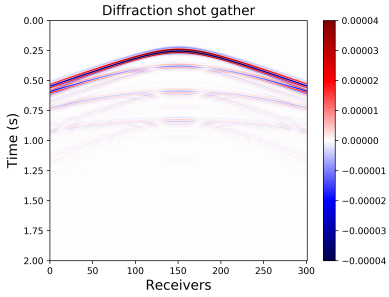

(i)

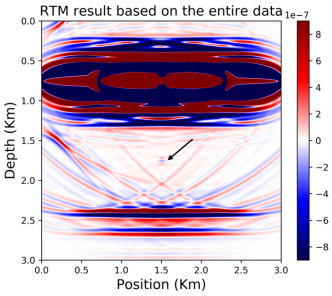

(j)

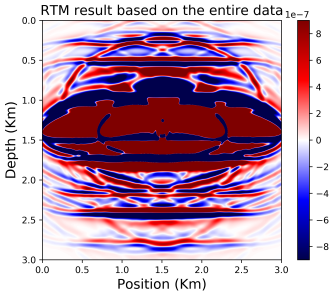

(k)

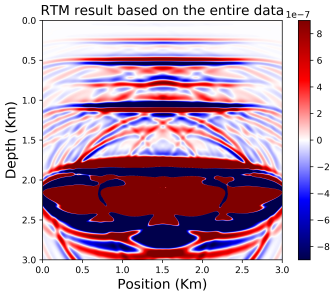

(l)

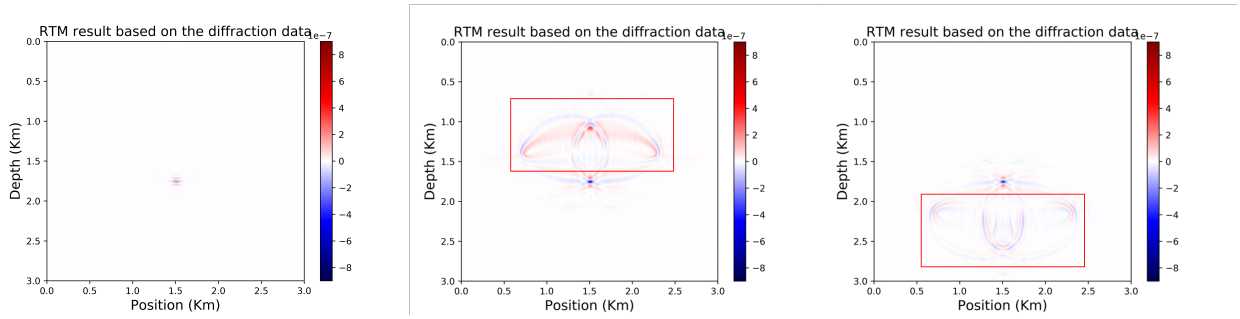

(m) (n) (o)

Figure 2.3: Three different layouts of the geometry in the same model and their corresponding seismic data and RTM imaging results. First row: Velocity models with different layouts of the geometries; Second row: Total shot gather generated from velocity model above; Third row: Diffraction shot gather; Fourth row: RTM results generated from the total shot gathers shown in the second row; Last row: RTM results generated from the diffraction shot gathers shown in the third row.

2.1.4 Factor III: Put the Sources and Receivers on the Same Side of the Point Scatterer

Allowing flexibility of the geometry opens up the possibility to further explore the case where the sources and receivers are on different sides of the point scatterers. In model 2.4b, the receivers are located on different sides of the scatterer point, at 0.75 km and 2.15 km respectively. From the total RTM result 2.4k, we find the second layer between the sources and the receivers is no longer imaged. This is because the information of the second layer recorded by the receivers is the transmitted energy and the RTM technique does not have the ability to handle the velocity anomaly information carried by the transmitted waves. From the diffraction RTM image 2.4m, we find the smearing of the point scatterer changes from laterally to vertically and the resolution declines as well.

Another example in which we place the sources and the receivers on different sides of the target is shown in model 2.4c. The total RTM image (2.4l) misses the second and the third layers between the sources and the receivers. The diffraction RTM result (2.4o) shows that the resolution of the diffraction image further decreases. Some of this decrease would be mitigated by using more sources, but we do not expect the basic result to change in that case.

In conclusion, if we are using RTM as the migration method, due to the limitation of this algorithm, when we relocate the sources and the receivers, they need to be on the same side of the target.

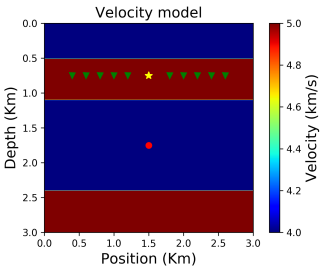

(a)

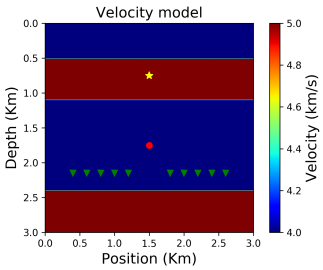

(b)

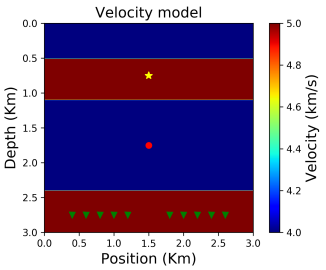

(c)

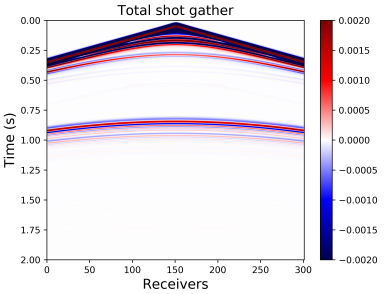

(d)

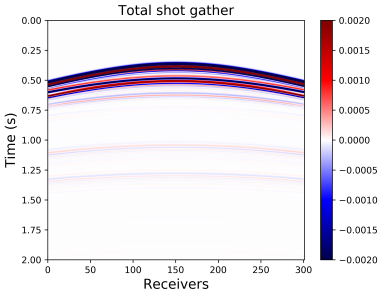

(e)

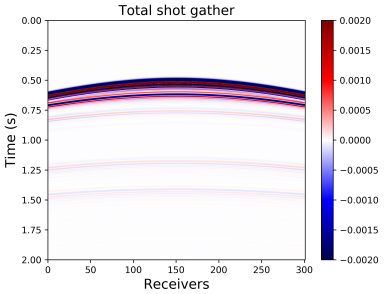

(f)

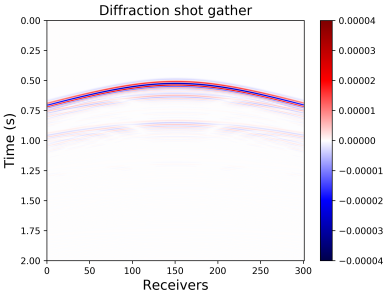

(g)

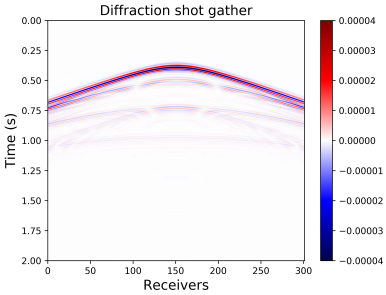

(h)

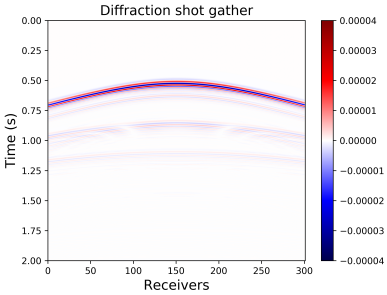

(i)

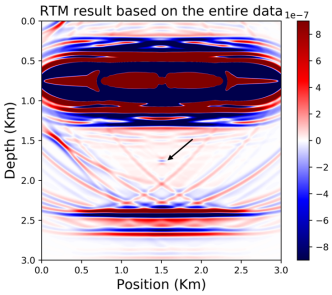

(j)

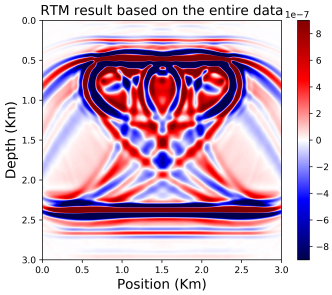

(k)

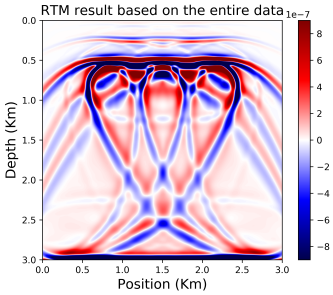

(l)

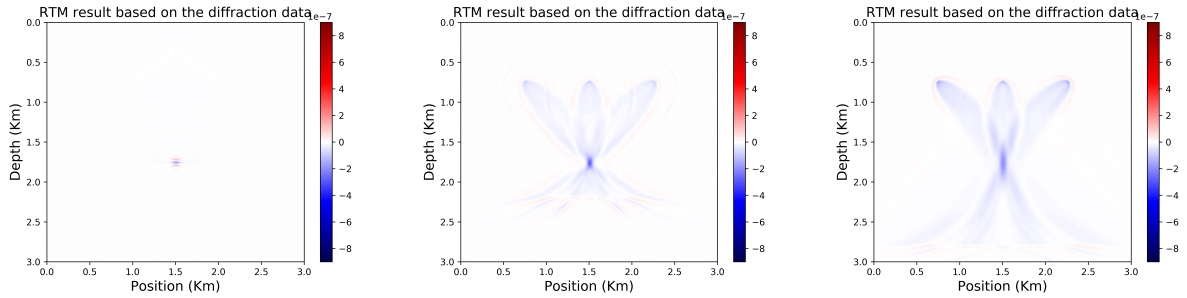

(m) (n) (o)

Figure 2.4: Three different layouts of the geometry in the same model and their corresponding seismic data and RTM imaging results. First row: Velocity models with different layouts of the geometries; Second row: Total shot gather generated from velocity model above; Third row: Diffraction shot gather; Fourth row: RTM results generated from the total shot gathers shown in the second row; Last row: RTM results generated from the diffraction shot gathers shown in the third row.

In conclusion, the depth of the sources and the receivers will affect the diffraction imaging. In order to better image the point scatterers, the sources and the receivers should be placed at the side of the point scatterer and near to it, but avoiding the source artifacts in RTM calculation at the same time.

2.2 Acquisition Surfaces Placed as Semicircles

Unlike specular reflections, diffractions do not satisfy Snell's law but act like secondary sources when the waves hit them, which means if we locate the receivers on a circle, the diffraction events will be straight lines on the shot gather. Starting from this assumption, in this section we set up a series of forward modelling models with receivers locating on a semi-circle to prove our guess.

2.2.1 Explanation of the Model

In this section, we explain the models and the data generated from them. Figure 2.5a is the velocity model with four layers and one point scatterer. The parameters of this model are the same as that in the previous section. The source is located at 2.15 km in depth, denoted as the yellow star. There are 40 receivers located on a half circle, denoted as green triangles. The radius of the circle is 0.4 km. Figure 2.5b is the velocity model without the point scatterer. Figure 2.5c is the shot gather recorded by the semicircular receivers based on model 2.5a. The first specular event is reflected from the third interface. The shape of the second and the third specular events are different from the normal hyperbolic events because of the unusual receiver layout. Subtracting the shot gather computed in model 2.5a from that computed in model 2.5b leads to the pure diffraction shot gather (Figure 2.5d). Notice that for visualization purposes, the amplitude ranges of total and diffraction shot gathers are different. The diffracted energy is still weak and cannot be distinguished clearly from the total shot gather. Figure 2.5e is the RTM result migrated from the total shot gather (Figure 2.5c). We can barely see the point scatterer on this image. Figure 2.5f is the RTM result migrated from pure diffractive shot gather. The point scatterer is clearly delineated and no extra reflectors are imaged.

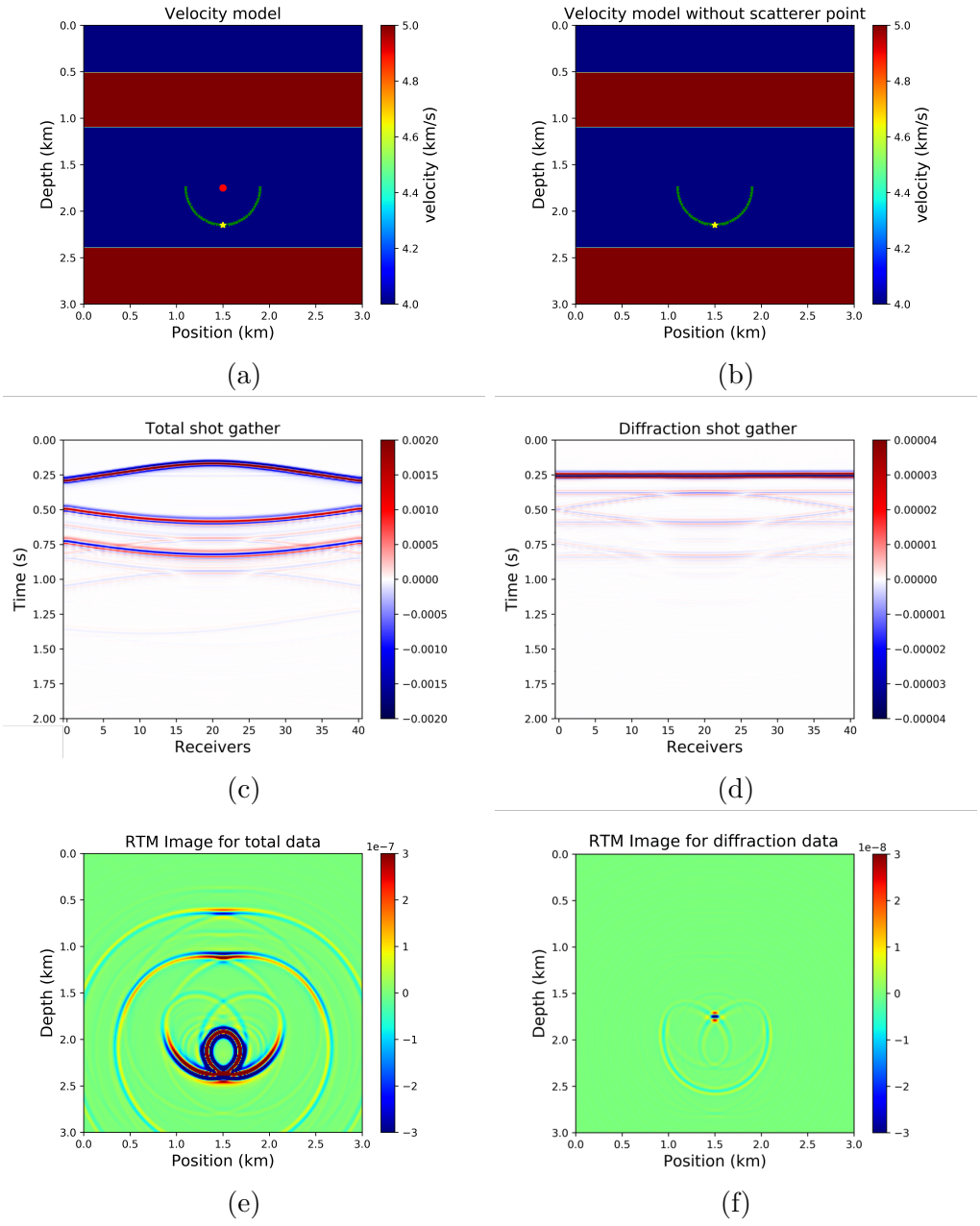

Figure 2.5: (a) Velocity model with point scatterer and receivers located in a semi-circle. (b) Velocity model without point scatterer. (c) Total shot gather generated from velocity model (a). (d) Diffraction shot gather generated by subtracting the reflection shot gather from the total shot gather. (e) The RTM result generated from the total shot gather (c). (f) RTM result generated from the diffraction shot gather (d).

2.2.2 Enhance the Diffraction Imaging with F-k Filter and Variance Filter

Because the diffractions and the reflections have different slopes, in this section, we use an f-k filter and a variance filter to separate them. The f-k filter removes the events which are not flat and the variance filter further reduces the residual of these events.

The 2D Fourier transform is a strategy to decompose shot gather into plane-wave components. Different components have their characteristic propagating frequency and dip angle. Therefore, conducting a 2D Fourier transform of the seismic data along time and space variables allows us to separate the energy types in the f-k domain. A common application of f-k filter is to suppress linear noise with a dip filter. In this case, we will us it to separate our flat diffracted events. Figure 2.6 is a clear illustration explaining how ten events withdifferent trace dip angles are mapped into the f-k domain. Notice that for the flat event whose dipping angle is 0 ms/trace, the mapped signals will focus where the wavenumber is zero.

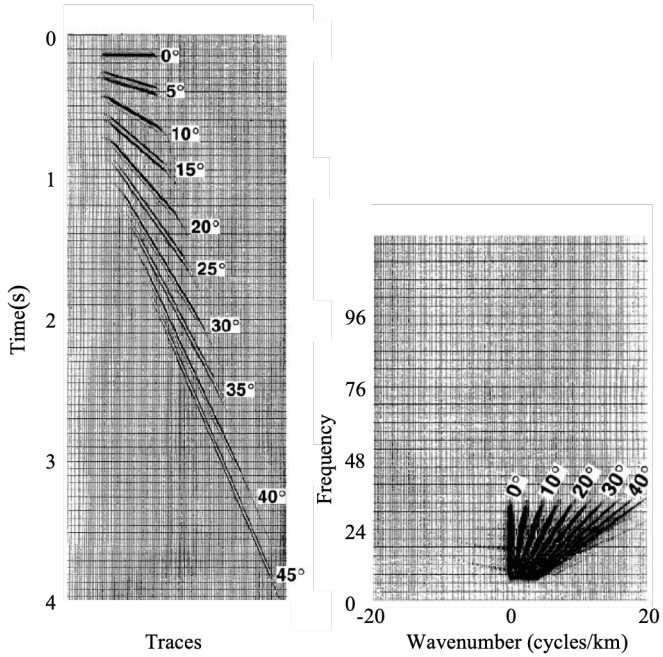

Figure 2.6: A zero-offset section containing 10 dipping events and its 2-D amplitude spectrum. (Yilmaz, 2001).

Figure 2.7a is the 2D Fourier transformation of Figure 2.5c, and Figure 2.7b is the 2D

Fourier transformation of Figure 2.5d. We see the energy of the diffraction event focusses at where the wavenumber is zero. In order to filter out the specular reflection event, we only keep the signal whose wavenumber is zero in the f-k domain (Figure 2.7c).

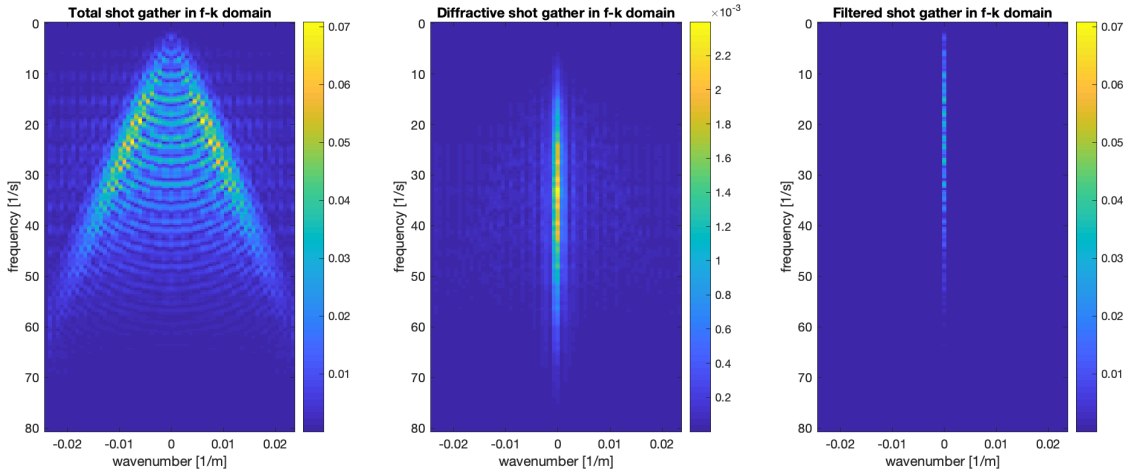

(a) (b) (c)

Figure 2.7: (a) The total shot gather (Figure 2.5c) in the f-k domain. (b) The diffraction shot gather (Figure 2.5d) in the f-k domain. (c) The filtered shot gather whose wavenumber is zero in the f-k domain.

Conducting the 2-D inverse fast Fourier transform to the filtered shot gather in f-k domain (Figure 2.7c) leads to Figure 2.8a. As we are basically keeping the events whose dipping angle is zero, we will also keep some parts of the specular energy which are flat in the shot gather (pointed out by red arrows in Figure 2.8a). In addition, there are some artifacts from the edge of the model (pointed out by blue arrows in Figure 2.8a). Figure 2.8c is the RTM image migrated from Figure 2.8a. At this time, we still cannot see the scattering point clearly from the filtered shot gather. However, we know that the energy of the diffractive event is stable and continuous over all of the receiver positions, while the energy of the specular event residual and the artifacts are not. So we simply calculate the variance of the data at each time sample and filter out those whose variance value is too large, then we get the further filtered shot gather (Figure 2.8b). The residual energy of the reflections are successfully filtered out, only the flat and continuous events remain. Figure 2.8d is the RTM image

calculated from Figure 2.8b. We see that the result is clear for the point scatterers. The artifacts from the receivers and the reflectors are effectively eliminated, and the diffraction energy is emphasized.

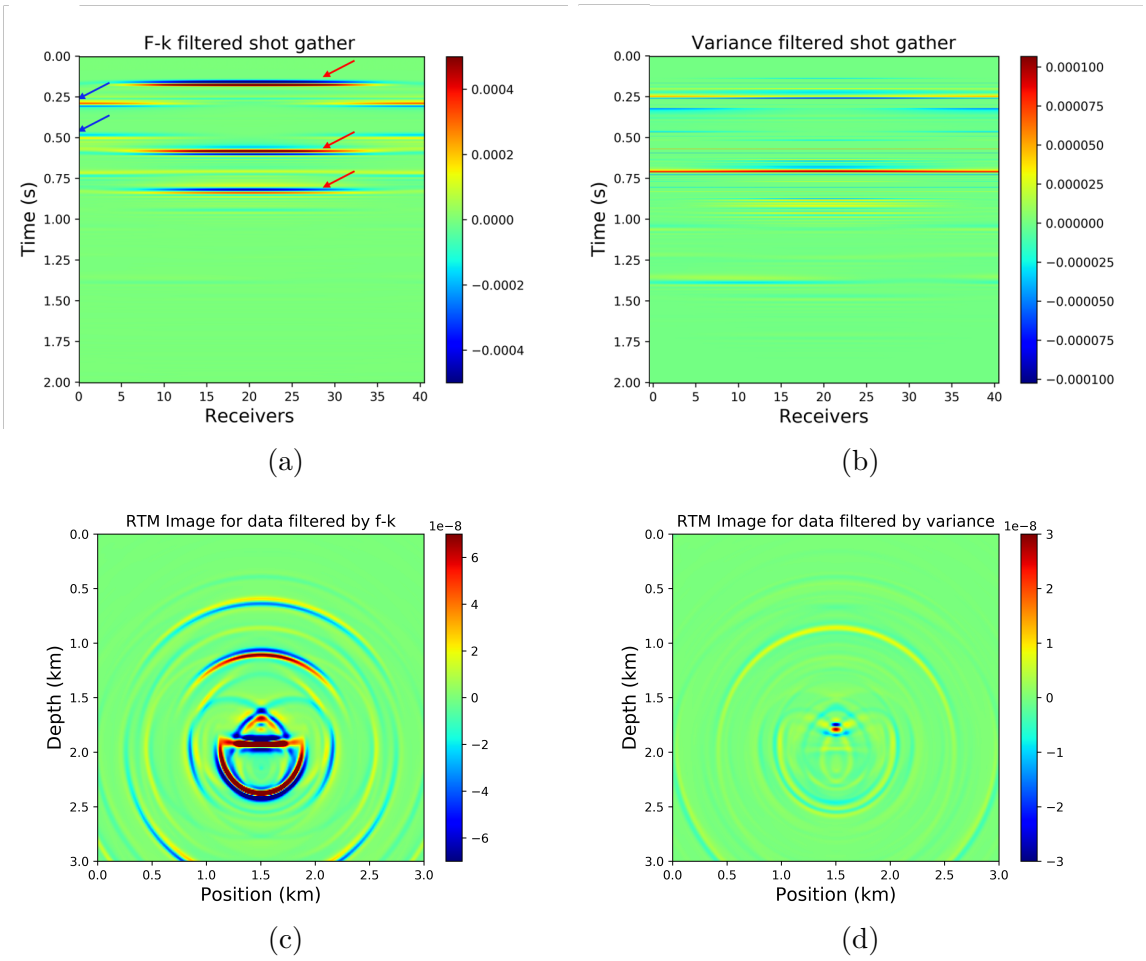

Figure 2.8: (a) Shot gather (Figure 2.7c) in the time domain. (b) The variance filtered shot gather based on the shot gather shown in Figure 2.8a. (c) The RTM result based on the shot gather shown in Figure 2.8a. (d) The RTM result based on the shot gather shown in Figure 2.8b.

Next, we are going to test the adaptability of this method by trying to migrate two point scatterers together. Figure 2.9a is the velocity model with two scatterer points, located at 1.75 km and 1.5 km in depth respectively, denoted as two red dots. The source and receivers are denoted as yellow stars and green triangles respectively. Figure 2.9b is the velocity model without point scatterers. Figure 2.9c is the total shot gather recorded by the two sets of

semicircular receivers, the discontinuity in the middle of the shot gather (pointed out by the green dotted line) is because of the depth difference between the two set of receivers. Figure 2.9d is the difference between the shot gathers computed in model 2.9a and model 2.9b. Figure 2.9e and 2.9f are the RTM images migrated from shot gather 2.9c and 2.9d respectively. Figure 2.9f is the ideal result for migrating the scatterer points, shown as a comparison for the later calculated diffraction imaging.

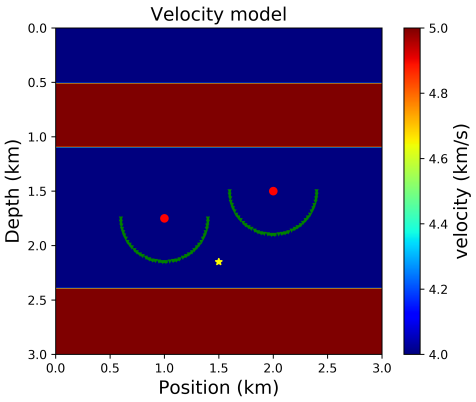

(a)

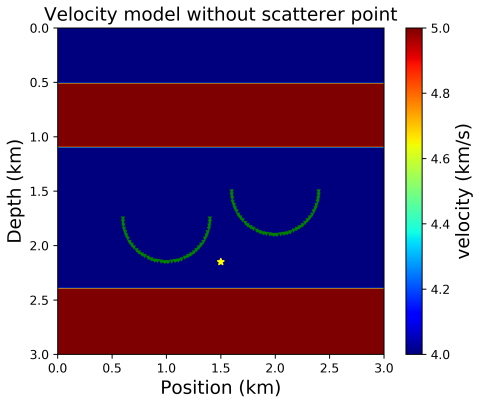

(b)

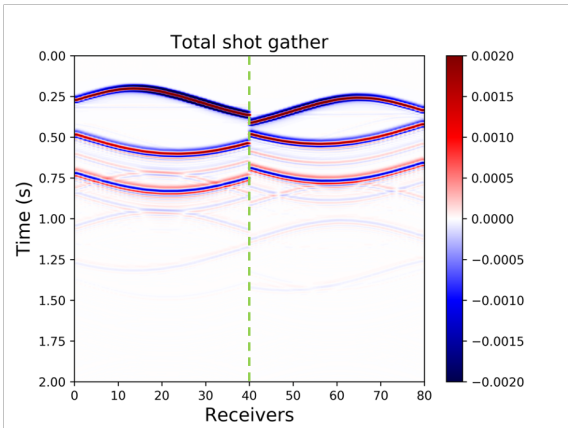

(c)

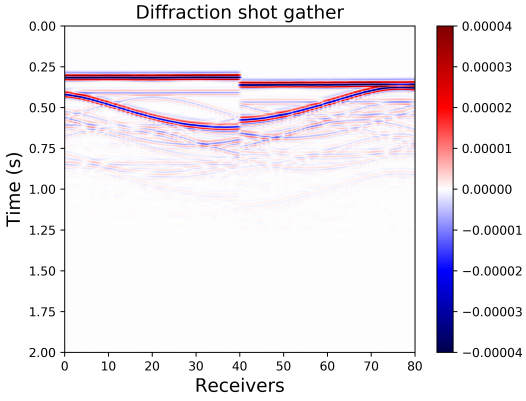

(d)

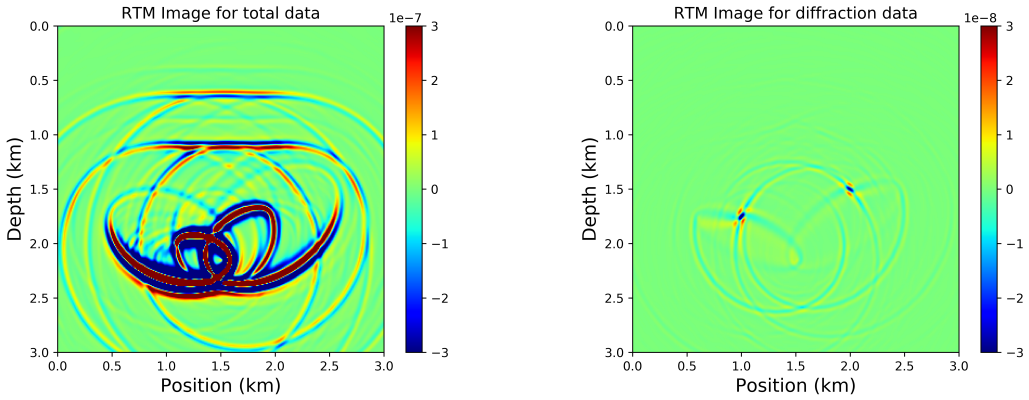

(e) (f)

Figure 2.9: (a) Velocity model with two point scatterers and receivers located in two semi-circles. (b) Velocity model without point scatterer. (c) Total shot gather generated from velocity model (a). (d) Diffraction shot gather generated by subtracting the reflection shot gather from the total shot gather. (e) The RTM result generated from the total shot gather (c). (f) RTM result generated from the diffraction shot gather (d).

In this model analysis, we have not shown the results of describing data in f-k domain. Filtering the data in f-k domain and transforming it back to time-space domain leads to Figure 2.10a. Based on the f-k filtered shot gather, we get the RTM image (see Figure 2.10c). In addition, we filter the data along each time sample limited by its variance value. The filtered shot gather and corresponding migrated result are shown by Figure 2.10b and 2.10d. Compared with Figure 2.9e or Figure 2.10c, the improvement of the diffraction imaging effect is significant, resulting in nearly the same image as the ideal result shown in Figure 2.9f.

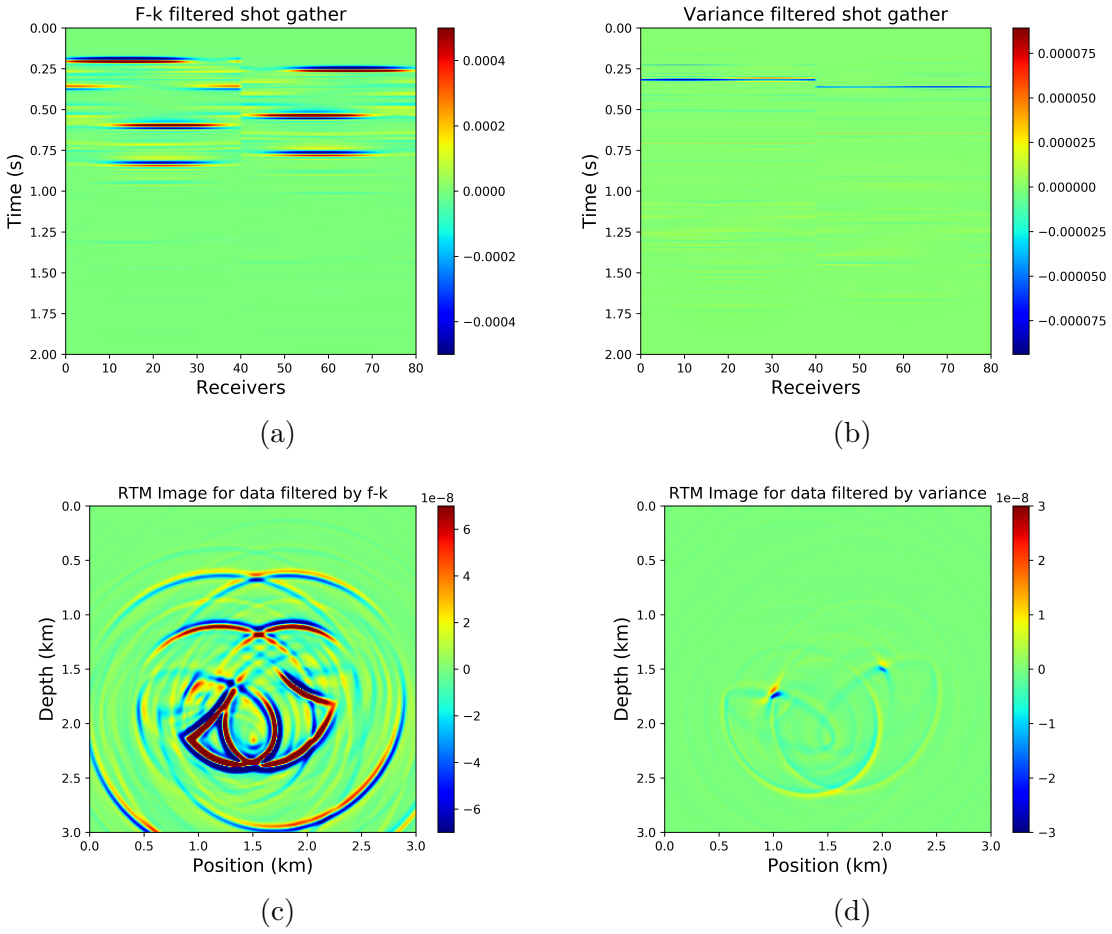

(a) (b) (c) (d)

Figure 2.10: (a) The f-k filtered shot gather. (b) The variance filtered shot gather. (d) The RTM result from the f-k filtered shot gather shown in Figure 2.10a. (d) The RTM result from the variance filtered shot gather shown in Figure 2.10d.

We further test the validity of the method by putting a point scatterer in the Marmousi velocity model (Figure 2.11a). Figure 2.11b is the difference between the shot gathers with and without the point scatterers. Figure 2.11c is the ideal diffraction imaging. Figure 2.11d is the processed result from the semicircular receivers. We see this method still suffers from a little dispersion problem, but overall the diffraction imaging is already quite delightful and the ability to eliminate the specular energy is excellent.

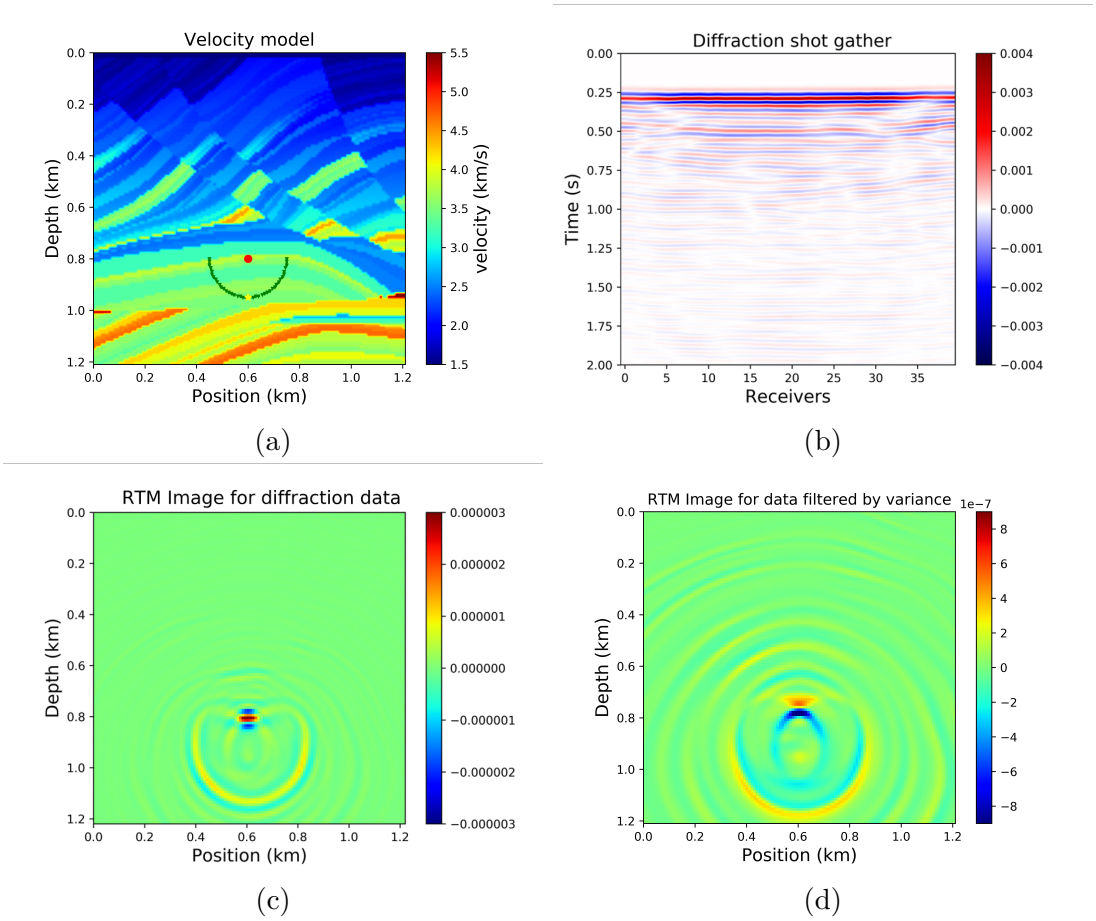

Figure 2.11: (a) The Marmousi velocity model with one point scatterer and the semi-circle located receivers. (b) The true diffraction shot gather generated from the forward modelling. (c) The RTM result from the true diffraction shot gather shown in Figure 2.11b. (d) The RTM result from the variance filtered shot gather.

In this chapter, we improve the diffraction imaging by changing the source/receiver layout. We first locate the receivers on a line in the subsurface at different depths to find the best source/receiver position for diffraction imaging. We investigate that, in this case to better image the diffractions, the sources and the receivers should be placed on the same side of the point scatterer and near to it, but avoiding being placed in the same layer with it in order to avoid the source artifacts in the RTM calculation. We also locate the receives on a semi-circle around the point scatterer and use the f-k filter and the variance filter to separate the diffractions and the reflections. This source/receiver layout gives a superior diffraction imaging result without the interference of the reflections. Notice that the placement of the

receivers as a semi-circle depends on knowing where the point scatterers are. The preferred models we choose in this chapter will be used in Chapter four.

Chapter 3

Green's Function Retrieval by Marchenko Equation

In this Chapter, I start by describing the theoretical foundations of the Marchenko equation. I derive how to iteratively solve the 1D Marchenko equation following the ideas proposed by Rose (2001). I further expand the Marchenko equation from 1D to 3D following the derivation given by Wapenaar et al. (2014). In the application part, I go through the procedure of conducting Marchenko redatuming with all of the necessary details, including the choosing of the source type and the wavelet, the generation of the reflection response, direct wave and window filter. The iterative solution to the coupled Marchenko equation is also derived because this is a key step in the retrieval of the Green's function. These will give future students a careful guide for conducting Marchenko imaging.

3.1 Solving 1D Marchenko Equation by Autofocusing

The Marchenko equation forms the basis of 1D inverse scattering theory (Marchenko, 1955). It has been widely used in mathematical physics to solve inverse scattering problems for more than 60 years. Lamb (1980) derived the 1D Marchenko equation with the help of the fundamental solution of Schrödinger's equation.

A critical step in the popularization of the Marchenko equation for solving seismic problems comes from Rose (2001). He proposes a single-sided autofocusing procedure to iteratively derive an incident wave, which focusses onto a particular point inside the model after a specific time interval. Theoretically, the desired incident wave is equal to the time-reversed solution of the Marchenko equation subtracted from a delta function. This opened up the possibility of solving the Marchenko equation iteratively. Rose (2001)'s work links inverse scattering and autofocusing together opening up the possibility of the application of the Marchenko equation in seismic imaging.

The 1D form of the Marchenko equation is:

$$0 = u(t, t_f) + R(t + t_f) + \int_{-\infty}^{+\infty} dt' R(t + t') u(t'; t_f)\,. \tag{3.1}$$

Equation 3.1 exactly describes the relationship between the reflected waves $R(t)$, which are measured from one side of the model, and the desired incident wavefield $u(t, t_f)$, which will focus inside the medium at a specific time, t_f, after it is emitted from the receiving surface (Broggini et al., 2012).

Next, I am going to derive how to iteratively get the solution of the Marchenko equation using autofocusing. The autofocusing iterative scheme proposed by Rose (2001) only requires the reflection response $R(t)$ measured at the boundary of the medium. Here I am going to go through the iterative scheme for two iterations, until I get an obvious and stable result.

First, send a delta function $\delta(t - x/c_0)$ into a 1D medium and measure the reflected 1D wavefield $R(t)$ at $x = 0$. Then $R(t)$ is regarded as the reflected coefficient to the unknown

velocity model. Thus, the reflected field measured at $x = 0$, $\varphi_{out}(t)$, is defined as a convolution of the incident field, $\varphi_{in}(t - x/c_0)$, and the reflected coefficient R,

$$\varphi_{out}(t) = \int_{-\infty}^{+\infty} dt' R(t - t')\varphi_{in}(t'). \tag{3.2}$$

Next we send in an initial incident pulse, $\varphi^1_{in}(x, t) = \delta(t + t_f - x/c_0)$, to start the iterative autofocusing scheme. Here, the initial incident pulse is designed to cross the origin of the coordinates ($x = 0$) at $t = -t_f$ and arrive at the focus point x_f at $t = 0$. Using equation 3.2, I obtain the initial reflected data:

$$\varphi^1_{out}(t, x) = \int_{-\infty}^{+\infty} dt' R(t - t')\delta(t' + t_f - x/c_0) = R(t + t_f - x/c_0). \tag{3.3}$$

Following the autofocusing steps in Rose (2001), I start the first step as follows:

Step 1: Evaluating the reflected wave at $x = 0$ gives

$$\varphi^1_{out}(t) = R(t + t_f)\,. \tag{3.4}$$

Using the window function Θ to truncate everything that arrives after t_f, equation 3.4 turns into:

$$\varphi^1_{out}(t) = R(t + t_f)\Theta(t_f - t). \tag{3.5}$$

Here, the window function $\Theta(x)$ is set to be one when $x \geqslant 0$ and zero when $x < 0$. We truncate the time because the incident and reflected waves are antisymmetric in time over $-t_f < t < t_f$, which is the key to autofocusing.

Step 2: Time reverse the reflected wave, turn t into $-t$, equation 3.5 becomes:

$$\varphi^1_{out}(-t) = R(-t + t_f)\Theta(t_f + t). \tag{3.6}$$

Prada et al. (1995) are the first to show that iteratively resending the time-reversed reflected

signal back into the medium will eventually make the whole wavefield focus on one point. In the Marchenko autofocusing scheme, time reversal is also a key point.

Step 3: Subtract equation 3.6 from $\delta(t+t_f)$ and obtain:

$$\delta(t+t_f)-\varphi^1_{out}(-t)=\delta(t+t_f)-R(-t+t_f)\Theta(t_f+t). \tag{3.7}$$

Step 4: Bring the position variable x back, let $t\to t-x/c_0$, resulting in a new incident pulse:

$$\varphi^2_{in}(t,x)=\delta(t-x/c_0+t_f)-R(-t+x/c_0+t_f)\Theta(t_f+t-x/c_0). \tag{3.8}$$

Steps 3 and 4 essentially use the first time-reversed reflected wave to update the second incident wave. The negative time-reversed reflected wave becomes the coda wave following the delta pulse.

In all, the updated incident wave is set to be the delta function minus time-reversed and time-truncated reflected wave.

So far, I have finished the first iteration, but the expression of the result and the relation between autofocusing and Marchenko equation are not clear yet. To clarify these relationships, I derive the second and the third iteration below:

Inserting the new incident wave 3.8 back into equation 3.2 gives (i.e. re-inserting our new estimated focussing wave into the Marchenko equation) the new reflected wave:

$$\begin{aligned}\varphi^2_{out}(t,x)&=\int_{-\infty}^{+\infty}dt'R(t-t')\{\delta(t'-x/c_0+t_f)-R(-t'+x/c_0+t_f)\Theta(t'-x/c_0+t_f)\}\\&=R(t-x/c_0+t_f)-\int_{-\infty}^{+\infty}dt'R(t-t')R(-t'+x/x_0+t_f)\Theta(t'-x/x_0+t_f).\end{aligned} \tag{3.9}$$

Step 1: Evaluating the result at $x = 0$, turns equation 3.9 into:

$$\begin{aligned}\varphi^2_{out}(t) &= R(t+t_f) - \int_{-\infty}^{+\infty} dt' R(t-t') R(-t'+t_f)\Theta(t'+t_f) \\ &= R(t+t_f) - \int_{-t_f}^{+\infty} dt' R(t-t') R(-t'+t_f) \\ &= R(t+t_f) - \int_{-\infty}^{+t_f} dt' R(t+t') R(t'+t_f).\end{aligned} \tag{3.10}$$

Truncating $t > t_f$, equation 3.10 turns into

$$\varphi^2_{out}(t) = R(t+t_f)\Theta(t_f - t) - \Theta(t_f - t)\int_{-\infty}^{t_f} dt' R(t+t') R(t'+t_f). \tag{3.11}$$

Step 2: Time reverse the result, $t \to -t$, equation 3.11 turns into:

$$\varphi^2_{out}(-t) = R(-t+t_f)\Theta(t_f + t) - \Theta(t_f + t)\int_{-\infty}^{t_f} dt' R(-t+t') R(t'+t_f). \tag{3.12}$$

Step 3: Subtracting equation 3.12 from $\delta(t+t_f)$ gives:

$$\delta(t+t_f) - \varphi^2_{out}(-t) = \delta(t+t_f) - R(-t+t_f)\Theta(t_f+t) + \Theta(t_f+f)\int_{-\infty}^{t_f} dt' R(-t+t') R(t'+t_f). \tag{3.13}$$

Step 4: Let $t \to t - x/c_0$, the result is the new incident pulse:

$$\begin{aligned}\varphi^3_{in}(t,x) =& \delta(t - x/c_0 + t_f) - R(-t + x/c_0 + t_f)\Theta(t - x/c_0 + t_f) \\ &+ \Theta(t_f + t - x/c_0)\int_{-\infty}^{t_f} dt' R(-t + t' + x/c_0) R(t'+t_f).\end{aligned} \tag{3.14}$$

Inserting equation 3.14 back into equation 3.2 gives:

$$\begin{aligned}
\varphi^3_{out}(t,x) &= \int_{-\infty}^{+\infty} dt' R(t-t')\varphi^3_{in}(t') \\
&= \int_{-\infty}^{+\infty} dt' R(t-t')\delta(t'-x/c_0+t_f) \\
&- \int_{-\infty}^{+\infty} dt' R(t-t')R(-t'+x/c_0+t_f)\Theta(t'-x/c_0+t_f) \\
&+ \int_{-\infty}^{+\infty} dt' R(t-t')\Theta(t'-x/c_0+t_f)\int_{-\infty}^{t_f} dt'' R(-t'+x/c_0+t'')R(t''+t_f) \\
&= R(t-x/c_0+t_f) - \int_{x/c_0-t_f}^{+\infty} dt' R(t-t')R(-t'+x/c_0+t_f) \\
&+ \int_{x/c_0-t_f}^{+\infty} dt' R(t-t')\int_{-\infty}^{t_f} dt'' R(-t'+x/c_0+t'')R(t''+t_f).
\end{aligned} \tag{3.15}$$

Evaluate the reflected data $\varphi^3_{out}(t,x)$ at $x=0$, equation 3.15 turns into:

$$\begin{aligned}
\varphi^3_{out}(t) &= R(t+t_f) - \int_{-t_f}^{+\infty} dt' R(t-t')R(-t'+t_f) \\
&+ \int_{-t_f}^{+\infty} dt' R(t-t')\int_{-\infty}^{t_f} dt'' R(-t'+t'')R(t''+t_f) \\
&= R(t+t_f) - \int_{-\infty}^{t_f} dt' R(t+t')R(t'+t_f) \\
&+ \int_{-\infty}^{t_f} dt' R(t+t')\int_{-\infty}^{t_f} dt'' R(t'+t'')R(t''+t_f).
\end{aligned} \tag{3.16}$$

At this point, we finish the second iteration. If we repeat $\varphi^1_{out}(t)$ (equation 3.4), $\varphi^2_{out}(t)$ (equation 3.10) and $\varphi^3_{out}(t)$ (equation 3.16) and analyze the inner relation between them, we obtain:

$$\begin{aligned}
&\varphi^1_{out}(t) = R(t+t_f)\,, \\
&\varphi^2_{out}(t) = R(t+t_f) - \int_{-\infty}^{t_f} dt' R(t+t')R(t'+t_f) = R(t+t_f) - \int_{-\infty}^{t_f} dt' R(t+t')\varphi^1_{out}(t')\,, \\
&\varphi^3_{out}(t) = R(t+t_f) - \int_{-\infty}^{t_f} dt' R(t+t')R(t'+t_f) + \int_{-\infty}^{t_f} dt' R(t+t')\int_{-\infty}^{t_f} dt'' R(t'+t'')R(t''+t_f)\,, \\
&\qquad = R(t+t_f) - \int_{-\infty}^{t_f} dt' R(t+t')\varphi^2_{out}(t')\,.
\end{aligned} \tag{3.17}$$

Generalizing equation 3.17, gives the integral equation:

$$\varphi_{out}^{n}(t;t_f) = R(t+t_f) - \int_{-\infty}^{t_f} dt' R(t'+t)\varphi_{out}^{n-1}(t';t_f). \tag{3.18}$$

The form of equation 3.18 is nearly same as Marchenko's integral equation 3.1. If we simply change $\varphi_{out}(t;t_f)$ into $-u(t;t_f)$, in the equation 3.18 we obtain:

$$0 = u(t;t_f) + R(t+t_f) + \int_{-\infty}^{+\infty} dt' R(t+t')u(t';t_f), \tag{3.19}$$

which is the Marchenko integral equation. $u(t;t_f)$ is the solution of the Marchenko equation, which we have obtained using an iterative procedure (equation 3.18) that requires us to measure only the reflected pulse. In conclusion, this "autofocusing" method (Rose, 2001) solves the Marchenko equation by regarding a delta function $\delta(t,t_f)$ as the initial input to start the iterative procedure described above. After several iterations, it converges to a wave field that solves the Marchenko equation.

3.2 3D Extension of Marchenko Equation

It is Wapenaar et al. (2013) who first derived the 3D Marchenko equation, which describes the relation between the single-sided reflected wavefield of a 3D medium and a field inside the medium. In this section, I am going to follow the derivation in Wapenaar et al. (2014) and explain the physical principles of the 3D Marchenko equation. The derivation starts with the one-way reciprocity theorem, which is used to derive relations between focusing functions and the Green's functions. Subsequently, based on the estimate we have of the Green's functions, we find an integral equation for the focusing function with reflection and transmission coefficients, which is our final target of this section.

3.2.1 Reciprocity Theorem for One-way Wave Field

Reciprocity theorems for one-way wave fields are the basis for deriving particular formulas relating different Green's functions. They play an important role in generating the single-sided 3D Marchenko equation (Wapenaar et al., 2014).

Here two types of reciprocity theorems in the space-frequency domain are shown which are used in following derivation. First is the time convolution type:

$$\int_{\partial\mathbb{D}_0} \{p_A^+ p_B^- - p_A^- p_B^+\} d\mathbf{x}_0 = \int_{\partial\mathbb{D}_i} \{p_A^+ p_B^- - p_A^- p_B^+\} d\mathbf{x}_i, \tag{3.20}$$

where p is the acoustic pressure, the downward and upward propagating constituents of p are denoted by p^+ and p^-, respectively. p_A and p_B refer to two independent acoustic states. The spatial coordinate vector $\mathbf{x}$ is defined as $\mathbf{x} = (\mathbf{x}_H, x_3)$ where $\mathbf{x}_H = (x_1, x_2)$ is the horizontal coordinate vector and x_3 is the vertical coordinate. In this work, the positive x_3-axis is pointing downward. $\partial\mathbb{D}_0$ is an acoustically transparent boundary separating the upper homogeneous half-space and the lower actual inhomogeneous medium at depth level $x_3 = x_{3,0}$ (Figure3.1). Here we consider the boundary $\partial\mathbb{D}_0$ to be a free surface. The boundary $\partial\mathbb{D}_i$ is an arbitrary boundary chosen at depth level $x_3 = x_{3,i}$, with $x_{3,i} > x_{3,0}$.

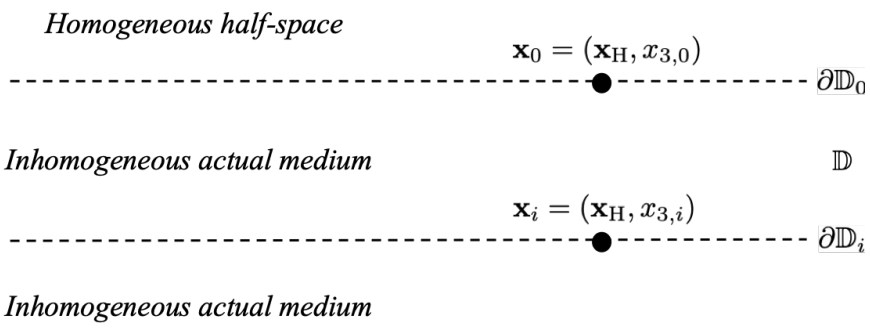

Figure 3.1: Illustration of the coordinates, boundaries and the medium.

Coordinates at $\partial\mathbb{D}_0$ are denoted as $\mathbf{x}_0 = (\mathbf{x}_H, x_{3,0})$. Similarly, the coordinates at $\partial\mathbb{D}_i$ are denoted as $\mathbf{x}_i = (\mathbf{x}_H, x_{3,i})$. The medium between boundaries $\partial\mathbb{D}_0$ and $\partial\mathbb{D}_i$ is denoted as $\mathbb{D}$. The reason to refer to equation 3.20 as a convolution type is because products like $p_A^+ p_B^-$ in the frequency domain correspond to convolutions in the time domain. The reciprocity relationship of the time correlation type is

$$\int_{\partial\mathbb{D}_0} \{(p_A^+)^* p_B^+ - (p_A^-)^* p_B^-\} d\mathbf{x}_0 = \int_{\partial\mathbb{D}_i} \{(p_A^+)^* p_B^+ - (p_A^-)^* p_B^-\} d\mathbf{x}_i, \tag{3.21}$$

where the asterisk indicates the complex conjugation, being equivalent to time reversal in the time domain. Similar to the convolution type, the reason for regarding equation 3.21 as a correlation type relation is that products like $(p_A^+)^* p_B^+$ in the frequency domain correspond to correlations in the time domain.

The reciprocity theorems 3.20 and 3.21 are used to derive relations between focusing functions and the Green's function of the inhomogeneous medium in $\mathbb{D}$.

3.2.2 Focusing Functions

The fundamental solutions of Schrödinger's equation play an important role in deriving the 1D Marchenko equation (Lamb, 1980). Here, the fundamental solutions are expanded to 3D and renamed as focusing functions to better reveal the "focusing" property of these functions. Notice that the focusing functions describe acoustic wave states in a reference medium (Figure 3.2), where the part above boundary $\partial\mathbb{D}_i$ is the same as the inhomogeneous medium discussed in Figure 3.1 but the the medium below boundary $\partial\mathbb{D}_i$ is modeled as reflection-free. A schematic illustrating the focusing functions is shown in Figure 3.2.

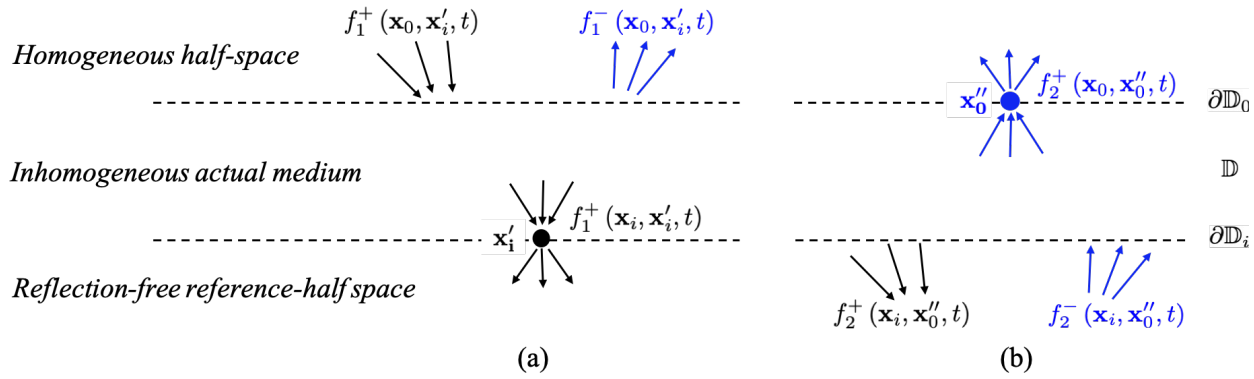

Figure 3.2: 3D focusing functions in a reference configuration. (a) The focusing function f_1 focuses at $\mathbf{x}_i' = (\mathbf{x}_H', x_{3,i})$ at $t = 0$. (b) The focusing function f_2 focuses at $\mathbf{x}_0'' = (\mathbf{x}_H'', x_{3,0})$ at $t = 0$.

The first focusing function $f_1(\mathbf{x}, t)$ consists of a down-going wave $f_1^+(\mathbf{x}, t)$ and a up-going wave $f_1^-(\mathbf{x}, t)$ in the homogeneous half space, with a relation like $f_1(\mathbf{x}, t) = f_1^+(\mathbf{x}, t) + f_1^-(\mathbf{x}, t)$. In the actual inhomogeneous medium, the down-going wavefield $f_1^+(\mathbf{x}, t)$ propagates and focusses on the focal point $\mathbf{x}_i'$ at boundary $\partial\mathbb{D}_i$ at $t = 0$ as a delta function in space and time. The boundary $\partial\mathbb{D}_i$ is called the focusing level. We denote the location of the focus point by $\mathbf{x}_i'$ and update the notation for the focussing function to include this location to $f_1^\pm(\mathbf{x}, \mathbf{x}_i', t)$. As show in Figure 3.2a, the down-going field $f_1^+(\mathbf{x}, \mathbf{x}_i', t)$ fully represents $f_1(\mathbf{x}, \mathbf{x}_i', t)$ at $\mathbf{x}_i' = (\mathbf{x}_H', x_{3,i})$ at $t = 0$. So the first focusing function is defined by spatial and time delta functions as:

$$f_1(\mathbf{x}_H, x_3 = x_{3,i}, t) = \delta(\mathbf{x}_H - \mathbf{x}_H')\delta(t). \tag{3.22}$$

The second focusing function contains both a down-going and a up-going wave in the reflection-free reference medium and finally focusses at focal point $\mathbf{x}_0''$ on boundary $\partial\mathbb{D}_0$ at $t = 0$. Similarly, f_2 is described as

$$f_2(\mathbf{x}_H, x_3 = x_{3,0}, t) = \delta(\mathbf{x}_H - \mathbf{x}_H'')\delta(t)\,. \tag{3.23}$$

In the frequency domain, the first focusing function is written as

$$f_1(\mathbf{x}, \mathbf{x}_i', \omega) = f_1^+(\mathbf{x}, \mathbf{x}_i', \omega) + f_1^-(\mathbf{x}, \mathbf{x}_i', \omega), \tag{3.24}$$

with $f_1^-(\mathbf{x}, \mathbf{x}_i', \omega) = 0$ under and on boundary $\partial\mathbb{D}_i$ ($x_3 \geq x_{3,i}$). Thus on boundary $\partial\mathbb{D}_i$, f_1 is expressed as

$$f_1(\mathbf{x}_i, \mathbf{x}_i', \omega) = f_1^+(\mathbf{x}_i, \mathbf{x}_i', \omega) = \delta(\mathbf{x}_H - \mathbf{x}_H'), \tag{3.25}$$

similarly, the form of f_2 is

$$f_2(\mathbf{x}, \mathbf{x}_0'', \omega) = f_2^+(\mathbf{x}, \mathbf{x}_0'', \omega) + f_2^-(\mathbf{x}, \mathbf{x}_0'', \omega), \tag{3.26}$$

$$f_2(\mathbf{x}_0, \mathbf{x}_0'', \omega) = f_2^-(\mathbf{x}_0, \mathbf{x}_0'', \omega) = \delta(\mathbf{x}_H - \mathbf{x}_H''). \tag{3.27}$$

Here I recall reciprocity theorems equation 3.20 and 3.21, to find the relations between f_1 and f_2 at the boundaries $\partial\mathbb{D}_0$ and $\partial\mathbb{D}_i$. Substituting $p_A^{\pm}(\mathbf{x}, \omega) = f_1^{\pm}(\mathbf{x}, \mathbf{x}_i', \omega)$ and $p_B^{\pm}(\mathbf{x}, \omega) = f_2^{\pm}(\mathbf{x}, \mathbf{x}_0'', \omega)$ into equations 3.20 and 3.21 leads to

$$\begin{aligned}
&\int_{\partial\mathbb{D}_0} \{f_1^+(\mathbf{x}, \mathbf{x}_i', \omega) f_2^-(\mathbf{x}, \mathbf{x}_0'', \omega) - f_1^-(\mathbf{x}, \mathbf{x}_i', \omega) f_2^+(\mathbf{x}, \mathbf{x}_0'', \omega)\} d\mathbf{x}_0 \\
&= \int_{\partial\mathbb{D}_i} \{f_1^+(\mathbf{x}, \mathbf{x}_i', \omega) f_2^-(\mathbf{x}, \mathbf{x}_0'', \omega) - f_1^-(\mathbf{x}, \mathbf{x}_i', \omega) f_2^+(\mathbf{x}, \mathbf{x}_0'', \omega)\} d\mathbf{x}_i,
\end{aligned} \tag{3.28}$$

Recall the property of $f_2^-(\mathbf{x}, \mathbf{x}_0'', \omega) = \delta(\mathbf{x}_H - \mathbf{x}_H'')$ and $f_2^+(\mathbf{x}, \mathbf{x}_0'', \omega) = 0$ at boundary $\partial\mathbb{D}_0$, as well as $f_1^+(\mathbf{x}_i, \mathbf{x}_i', \omega) = \delta(\mathbf{x}_H - \mathbf{x}_H')$ and $f_1^-(\mathbf{x}, \mathbf{x}_i', \omega) = 0$ at boundary $\partial\mathbb{D}_i$, equation 3.28

simplifies to

$$\int_{\partial\mathbb{D}_0} f_1^+(\mathbf{x}, \mathbf{x}_i', \omega)\delta(\mathbf{x}_H - \mathbf{x}_H'')d\mathbf{x}_0 = \int_{\partial\mathbb{D}_i} \delta(\mathbf{x}_H - \mathbf{x}_H')f_2^-(\mathbf{x}, \mathbf{x}_0'', \omega)d\mathbf{x}_i, \tag{3.29}$$

which reduces to

$$f_1^+(\mathbf{x}_0'', \mathbf{x}_i', \omega) = f_2^-(\mathbf{x}_i', \mathbf{x}_0'', \omega). \tag{3.30}$$

Similar to the derivation above, the second focusing function relationship is

$$-\{f_1^-(\mathbf{x}_0'', \mathbf{x}_i', \omega)\}^* = f_2^+(\mathbf{x}_i', \mathbf{x}_0'', \omega). \tag{3.31}$$

3.2.3 Green's Function Representations

Here, we are going to derive relationships between the focusing functions defined in the previous section and the one-way Green's function in the actual inhomogeneous medium $\mathbb{D}$, generated by a flux-normalized source (i.e. a delta function) located at $\mathbf{x}_0''$, just above $\partial\mathbb{D}_0$, see Figure 3.3.

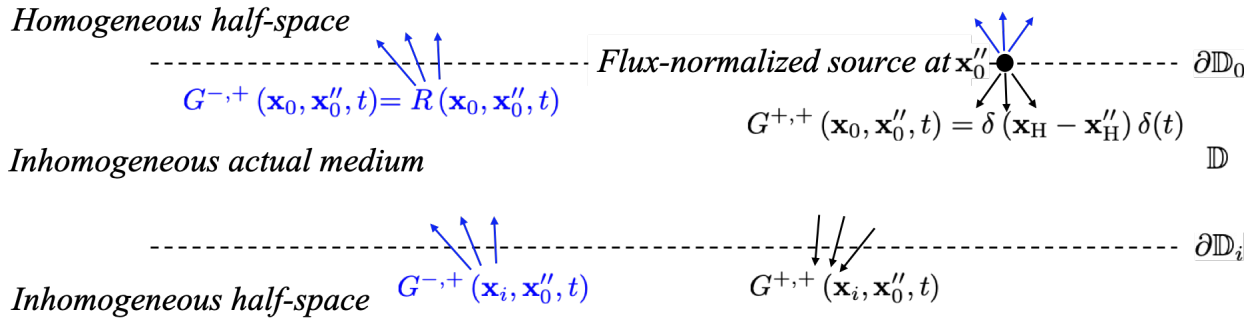

Figure 3.3: One-way Green's functions generated by flux-normalized source in the actual inhomogeneous medium. The Green's functions $G^{-,+}(\mathbf{x}_0, \mathbf{x}_0'', t)$ and $G^{+,+}(\mathbf{x}_0, \mathbf{x}_0'', t)$ denote the reflection response $R(\mathbf{x}_0, \mathbf{x}_0'', t)$ of the medium and the source, respectively.

At the source level, the downward propagating Green's function is described as the source function, given as

$$G^{+,+}(\mathbf{x}_0, \mathbf{x}_0'', t) = \delta(\mathbf{x}_H - \mathbf{x}_H'')\delta(t), \tag{3.32}$$

the first and the second superscript $(+)$ denote the downward propagation direction at the observation point $\mathbf{x}_0$ and the downward radiating part of the source at $\mathbf{x}_0''$, respectively. The upward propagating component of the Green's function at $\partial\mathbb{D}_0$ is actually the reflection response recorded at one side of the medium, defined as:

$$G^{-,+}(\mathbf{x}_0, \mathbf{x}_0'', t) = R(\mathbf{x}_0, \mathbf{x}_0'', t). \tag{3.33}$$

In the frequency domain, equations 3.32 and3.33 become:

$$G^{+,+}(\mathbf{x}_0, \mathbf{x}_0'', \omega) = \delta(\mathbf{x}_H - \mathbf{x}_H''), \tag{3.34}$$

and

$$G^{-,+}(\mathbf{x}_0, \mathbf{x}_0'', \omega) = R(\mathbf{x}_0, \mathbf{x}_0'', \omega). \tag{3.35}$$

Deriving expressions for the one-way Green's functions in terms of the focusing functions at the boundary $\partial\mathbb{D}_i$ requires us to regard the Green's functions and the focusing functions as the two independent states in the reciprocity relations. In addition, we will require the reciprocity of the source and receivers

$$R\left(\mathbf{x}_0, \mathbf{x}_0'', \omega\right) = R\left(\mathbf{x}_0'', \mathbf{x}_0, \omega\right) . \tag{3.36}$$

With the help of equations 3.25, 3.34, 3.35 and 3.36, substituting $p_A^{\pm}(\mathbf{x}, \omega) = f_1^{\pm}(\mathbf{x}, \mathbf{x_i'}, \omega)$ and $p_B^{\pm}(\mathbf{x}, \omega) = G^{\pm,+}(\mathbf{x}, \mathbf{x_0''}, \omega)$ into the reciprocity theorem equation 3.20 and 3.21 yields

$$\int_{\partial\mathbb{D}_0} f_1^{+}(\mathbf{x}_0, \mathbf{x}_i', \omega) R(\mathbf{x}_0'', \mathbf{x}_0, \omega) d\mathbf{x}_0 - f_1^{-}(\mathbf{x}_0'', \mathbf{x}_i', \omega) = G^{-,+}(\mathbf{x}_i', \mathbf{x}_0'', \omega), \tag{3.37}$$

and

$$-\int_{\partial\mathbb{D}_0} \{f_1^{-}(\mathbf{x}_0, \mathbf{x}_i', \omega)\}^* R(\mathbf{x}_0'', \mathbf{x}_0, \omega) d\mathbf{x}_0 + \{f_1^{+}(\mathbf{x}_0'', \mathbf{x}_i', \omega)\}^* = G^{+,+}(\mathbf{x}_i', \mathbf{x}_0'', \omega). \tag{3.38}$$

Adding equation 3.37 and 3.38, with the help of equations 3.26, 3.30 and 3.31, leads to

$$G^{+,+}(\mathbf{x}_i', \mathbf{x}_0'', \omega) + G^{-,+}(\mathbf{x}_i', \mathbf{x}_0'', \omega) = \int_{\partial\mathbb{D}_0} f_2(\mathbf{x}_i', \mathbf{x}_0, \omega) R(\mathbf{x}_0'', \mathbf{x}_0, \omega) d\mathbf{x}_0 + \{f_2(\mathbf{x}_i', \mathbf{x}_0'', \omega)\}^*. \tag{3.39}$$

The left hand side of equation 3.39 is the Green's functions, recording the data inside the medium which is excited on the acquisition surface. The right hand side of equation 3.39 consists of the reflection response, which records the data measured and excited on the acquisition surface, and the focusing function, which focusses on the acquisition surface. Equation 3.39 shows that via the focusing function, the data recorded on the surface can be redatumed to the subsurface.

3.2.4 3D Marchenko Equation

Transforming equation 3.39 to the time domain gives

$$G^{+,+}(\mathbf{x}_i', \mathbf{x}_0'', t) + G^{-,+}(\mathbf{x}_i', \mathbf{x}_0'', t) = \int_{\partial\mathbb{D}_0} \int_{-\infty}^{t} f_2(\mathbf{x}_i', \mathbf{x}_0, t') R(\mathbf{x}_0'', \mathbf{x}_0, t - t') dt' d\mathbf{x}_0 + f_2(\mathbf{x}_i', \mathbf{x}_0'', -t) \,. \tag{3.40}$$

The right hand side of equation 3.40 is used to derive the 3D Marchenko equation. If we express the first arrival time from source location $\mathbf{x}_0''$ to focal point $\mathbf{x}_i'$ as $t_d(\mathbf{x}_i', \mathbf{x}_0'')$ and constrain the time to be smaller than the first arrival time, then the left hand side of the equation should be zero. Equation 3.40 becomes

$$0 = \int_{\partial\mathbb{D}_0} \int_{-\infty}^{t} f_2(\mathbf{x}_i', \mathbf{x}_0, t') R(\mathbf{x}_0'', \mathbf{x}_0, t - t') dt' d\mathbf{x}_0 + f_2(\mathbf{x}_i', \mathbf{x}_0'', -t) \quad (t < t_d(\mathbf{x}_i', \mathbf{x}_0'')) \,. \tag{3.41}$$

Because of the causality property of the reflection coefficient $R(\mathbf{x}_0'', \mathbf{x}_0, t - t')$, the upper integration time limit becomes $t - t' > 0$. In integral equation 3.41, the reflection response R is the known response, measured at the acquisition surface. The focusing function f_2 is our unknown that we would like to determine.

Before we solve equation 3.41, another property of f_2 is discussed here. Recall the focusing property of f_2 shown in Figure 3.4a, if we put a flux-normalized source at the focal point $\mathbf{x}_0''$, we can record the transmission response $T(\mathbf{x}_i', \mathbf{x}_0'', t)$ of the actual inhomogeneous medium on boundary $\partial\mathbb{D}_0$ as illustrated in Figure 3.4b.

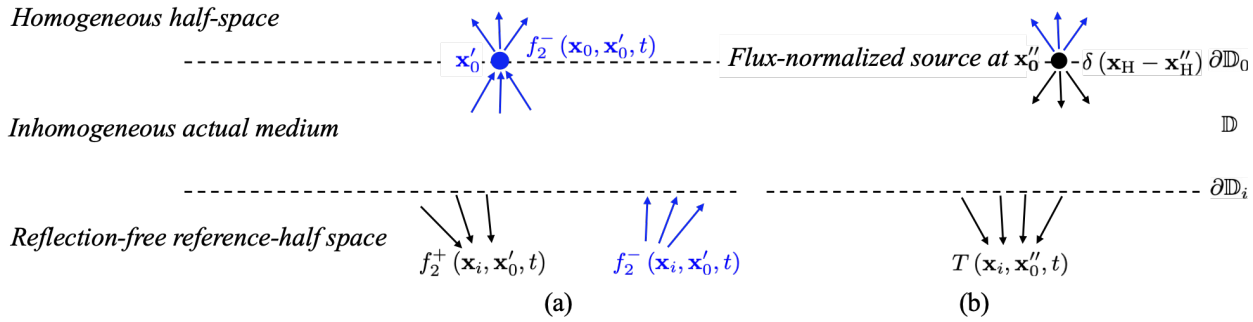

Figure 3.4: (a) The focusing function f_2 focuses at $\mathbf{x}_0' = (\mathbf{x}_H', x_{3,0})$ at $t = 0$. (b) Illustration of the transmission response generated by the flux-normalized source at $\mathbf{x}_0'' = (\mathbf{x}_H'', x_{3,0})$.

In order to derive the relationship between the focusing function f_2 and the transmission response, we need to use the acoustic state reciprocity equation 3.20 again. Equation 3.20 describe the acoustic states in frequency domain so we are going to write f_2 and T as below:

$$\begin{gathered} p_A^+\left(\mathbf{x}_0,\omega\right)=\delta\left(\mathbf{x}_H-\mathbf{x}_{\mathrm{H}}''\right)\,,\; p_A^+\left(\mathbf{x}_i,\omega\right)=T\left(\mathbf{x}_i,\mathbf{x}_0'',\omega\right)\,, \\ p_A^-\left(\mathbf{x}_i,\omega\right)=0\,, \\ p_B^{\pm}(\mathbf{x},\omega)=f_2^{\pm}\left(\mathbf{x},\mathbf{x}_0',\omega\right)\,. \end{gathered} \tag{3.42}$$

We have

$$\begin{aligned} &\int_{\partial\mathbb{D}_0}\{\delta(\mathbf{x}_H'-\mathbf{x}_H'')f_2^-(\mathbf{x}_0,\mathbf{x}_0',\omega)-p_A^-(\mathbf{x}_0,\omega)f_2^+(\mathbf{x}_0,\mathbf{x}_0',\omega)\}d\mathbf{x}_0 \\ &\quad=\int_{\partial\mathbb{D}_i}\{T\left(\mathbf{x}_i,\mathbf{x}_0'',\omega\right)f_2^-\left(\mathbf{x}_i,\mathbf{x}_0',\omega\right)-0\cdot f_2^+\left(\mathbf{x}_i,\mathbf{x}_0',\omega\right)\}d\mathbf{x}_i\,. \end{aligned} \tag{3.43}$$

Substituting equation 3.27 and $f_2^+(\mathbf{x}_0,\mathbf{x}_0',w)=0$ into equation 3.43, we have

$$\int_{\partial\mathbb{D}_0}\delta(\mathbf{x}_H'-\mathbf{x}_H'')\delta(\mathbf{x}_H'-\mathbf{x}_H')d\mathbf{x}_0=\int_{\partial\mathbb{D}_0}T(\mathbf{x}_i,\mathbf{x}_0'',\omega)f_2^-(\mathbf{x}_i,\mathbf{x}_0',\omega)d\mathbf{x}_i\,. \tag{3.44}$$

$$\delta\left(\mathbf{x}_H'-\mathbf{x}_H''\right)=\int_{\partial\mathbb{D}_0}T\left(\mathbf{x}_i,\mathbf{x}_0'',\omega\right)f_2^-\left(\mathbf{x}_i,\mathbf{x}_0',\omega\right)d\mathbf{x}_i\,. \tag{3.45}$$

Rewriting equation 3.45 into time domain, we have f_2^- denoted as the inverse of transmission response

$$f_2^-\left(\mathbf{x}_i,\mathbf{x}_0'',t\right)=T^{\mathrm{inv}}\left(\mathbf{x}_i,\mathbf{x}_0'',t\right)\,. \tag{3.46}$$

Lamb (1980) defines $f_2(x,t)$ in the 1D Marchenko case as a delta function followed by a coda wave caused by the scattering potential in the medium. Also recall the conclusion from Section 3.1, that the incident wave which focusses onto one point in the 1D medium is a delta function minus the time-reversed solution of the Marchenko equation. Therefore we can make a similar assumption about the form of f_2 in 3D. f_2 is the superposition of the direct

wave and the scattering coda, which is also the solution to the 3D Marchenko equation.

$$f_2(\mathbf{x}_i, \mathbf{x}_0'', t) = T_d^{inv}(\mathbf{x}_i, \mathbf{x}_0'', t) + M(\mathbf{x}_i, \mathbf{x}_0'', t), \tag{3.47}$$

where $M(\mathbf{x}_i, \mathbf{x}_0'', t)$ is the scattering coda following the direct arrival with $M(\mathbf{x}_i, \mathbf{x}_0'', t) = 0$ when $t \leq -t_d(\mathbf{x}_i, \mathbf{x}_0'')$. Substituting equation 3.47 into equation 3.41 yields

$$\begin{aligned}
&\int_{\partial\mathbb{D}_0} d\mathbf{x}_0 \int_{-\infty}^{-t_d^{\epsilon}(\mathbf{x}_i', \mathbf{x}_0)} T_d^{inv}(\mathbf{x}_i', \mathbf{x}_0, t') R(\mathbf{x}_0'', \mathbf{x}_0, t - t') dt' \\
&+ \int_{\partial\mathbb{D}_0} d\mathbf{x}_0 \int_{-t_d^{\epsilon}(\mathbf{x}_i', \mathbf{x}_0)}^{t} M(\mathbf{x}_i', \mathbf{x}_0, t') R(\mathbf{x}_0'', \mathbf{x}_0, t - t') dt' \\
&+ M(\mathbf{x}_i', \mathbf{x}_0'', -t) = 0 \qquad\qquad for \quad t < t_d(\mathbf{x}_i', \mathbf{x}_0''),
\end{aligned} \tag{3.48}$$

where $t_d^{\epsilon}(\mathbf{x}_i', \mathbf{x}_0) = t_d(\mathbf{x}_i', \mathbf{x}_0) - \epsilon$, with ϵ a small positive constant, introduced to make sure the direct arrival T is included in the first integral. Equation 3.48 is the 3D Marchenko equation. The input of this equation is the direct arrival and the reflection response. The reflection response $R(\mathbf{x}_0'', \mathbf{x}_0, t)$ is generated and recorded at the acquisition level. The direct arrival $T_d^{inv}(\mathbf{x}_i', \mathbf{x}_0, t')$ describes the wave state from sources $\mathbf{x}_0$ on boundary $\partial\mathbb{D}_0$ (acquisition level) to focusing point $\mathbf{x}_i'$. Based on the source and receiver reciprocity, the direct arrival could be calculated by forward modelling, putting a virtual source at the focal point $\mathbf{x}_i'$ and calculating the response at the receivers located at $\mathbf{x}_0$ on the acquisition level. A smoothed velocity model is sufficient to estimate T_d. The coda $M(\mathbf{x}_i', \mathbf{x}_0, t)$ is the solution to this integral equation. Working backwards, we can calculate focusing functions $f_2(\mathbf{x}_i', \mathbf{x}_0, t)$ using M and T_d^{inv}. Based on the relation of the focusing functions and the Green's function, we can get the Green's function as if the source is inside the medium, at the focusing point.

3.3 Green's Function Retrieval

In the first two parts of this section, we are going to discuss how to generate all of the input terms in equation 3.41, i.e., the reflection response R and the direct wave T_d. In the third part, we will go through the iterative procedure using these inputs to estimate the redatumed data, i.e., the coda M in equation 3.41.

3.3.1 Reflection Response

In this section I discuss how to generate a valid reflection response, which is the key to the convergence of the iterative procedure described in the previous sections. First, the source used to generate a reflection response should be a dipole source. Secondly, a unique wavelet and a scalar are applied to maintain the convergence of the algorithm from iteration to iteration.

3.3.1.1 Dipole Source

In the application of the Marchenko methodology, a number of researchers mention that the sought reflection response R is obtained from vertical dipole sources (Jia et al., 2018; Mildner et al., 2019; Ravasi et al., 2016). The dipole source consists of two monopoles of opposite sign but equal strength separated by a very small distance Δx (denoted as red and blue stars in Figure 3.5b). It can be approximated as the first derivative of the wavefield, generated by a monopole source, with respect to the vertical direction. Figure 3.5 shows the wave fields generated by the monopole source and dipole source respectively. The wave field emitted by a monopole source has equal energy at all directions while the one generated by dipole source is more focussed around the vertical direction. The theoretical reason why we use dipole source to generate the reflection response is derived below.

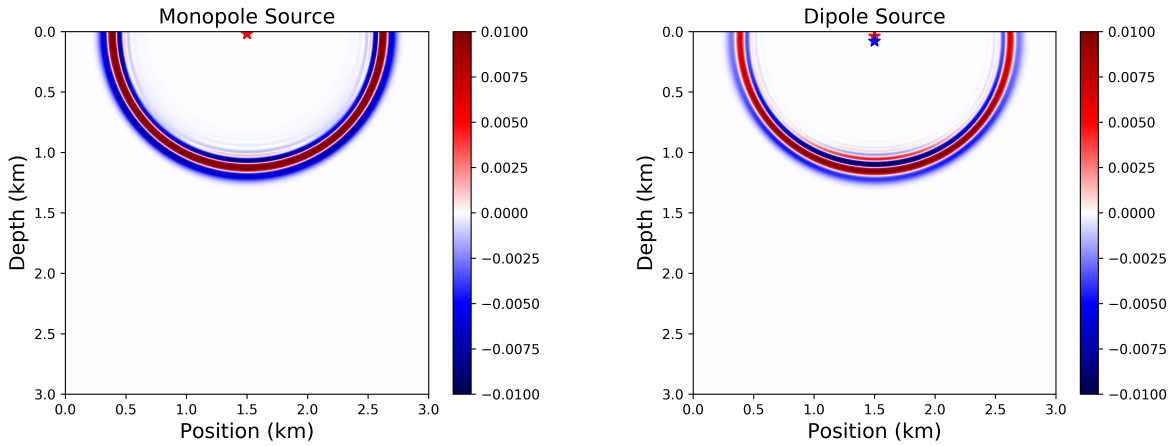

(a) (b)

Figure 3.5: Wavefield generated by (a) monopole source and (b) dipole source in a homogeneous model.

Notice that, the derivation we derived in section 3.2 are all based on the flux-normalized wave field assumption. In field applications, the data are recorded by pressure receivers, thus we use another pair of reciprocity theorems, which describe the pressure-normalized one-way wavefields, given as

$$-\int_{\partial\mathbb{D}_0}\rho^{-1}\left\{p_A^+\left(\partial_3 p_B^-\right)+p_A^-\left(\partial_3 p_B^+\right)\right\}\mathrm{d}\mathbf{x}_0=\int_{\partial\mathbb{D}_i}\rho^{-1}\left\{\left(\partial_3 p_A^+\right)p_B^-+\left(\partial_3 p_A^-\right)p_B^+\right\}\mathrm{d}\mathbf{x}_i\,. \tag{3.49}$$

$$-\int_{\partial\mathbb{D}_0}\rho^{-1}\left\{\left(p_A^+\right)^*\left(\partial_3 p_B^+\right)+\left(p_A^-\right)^*\left(\partial_3 p_B^-\right)\right\}\mathrm{d}\mathbf{x}_0=\int_{\partial\mathbb{D}_i}\rho^{-1}\left\{\left(\partial_3 p_A^+\right)^* p_B^+ +\left(\partial_3 p_A^-\right)^* p_B^-\right\}\mathrm{d}\mathbf{x}_i\,. \tag{3.50}$$

The pressure-normalized wave equation for Green's function is defined as

$$\rho\nabla\cdot\left(\frac{1}{\rho}\nabla G\right)-\frac{1}{c^2}\frac{\partial^2 G}{\partial t^2}=-\rho\delta\left(\mathbf{x}-\mathbf{x}_0''\right)\frac{\partial\delta(t)}{\partial t}\,. \tag{3.51}$$

The right hand of the equation indicates that an impulse source at $x=x_0''$ trigger the wave field at $t=0$. The pressure-normalized version of equation 3.34 is

$$\partial_3 G^{+,-}\left(\mathbf{x},\mathbf{x}_0'',\omega\right)\Big|_{x_3=x_{3,0}}=-\frac{1}{2}j\omega\rho\left(\mathbf{x}_0''\right)\delta\left(\mathbf{x}_\mathrm{H}-\mathbf{x}_\mathrm{H}''\right)\,. \tag{3.52}$$

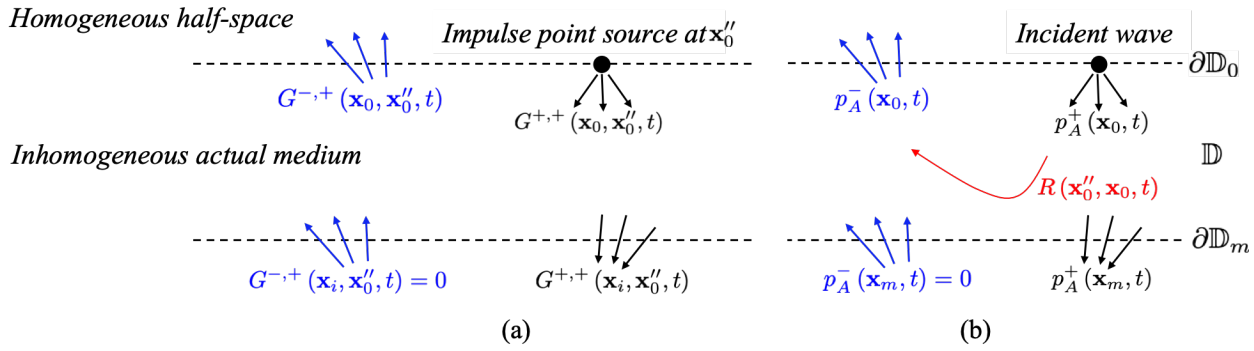

Figure 3.6: (a) Green's functions. (b) general acoustic wavefields.

To derive the relation of the Green's functions and the reflection response, we describe the Green's functions and general acoustic wavefields as the independent state A and B and relate them via the reciprocity relations in a different medium (Figure 3.6). Notice that the lower boundary $\partial\mathbb{D}_m$ is set to be lying below all the inhomogeneous medium so $p_A^-(\mathbf{x}_m, \omega) = p_B^-(\mathbf{x}_m, \omega) = 0$. $R(\mathbf{x}_0'', \mathbf{x}_0, \omega)$ is the reflection response for the down-going wave inside medium $\mathbb{D}$. For any incident field, the reflected field measured at $\partial\mathbb{D}_0$, is given by a convolution of the incident field and the reflection response. In frequency domain, we have

$$p_A^-(\mathbf{x}_0'', \omega) = \int_{\partial\mathbb{D}_0} R(\mathbf{x}_0'', \mathbf{x}_0, \omega)\, p_A^+(\mathbf{x}_0, \omega)\, \mathrm{d}\mathbf{x}_0\,. \tag{3.53}$$

Subsitituting $p_B^{\pm}(\mathbf{x}, \omega) = G^{\pm,+}(\mathbf{x}, \mathbf{x}_0'', \omega)$ into equation 3.49, we have

$$\int_{\partial\mathbb{D}_0} \rho^{-1}\{p_A^+(\mathbf{x}_0, w)\cdot\partial_3 G^{-,+}(\mathbf{x}_0, \mathbf{x}_0'', t) + p_A^-(\mathbf{x}_0, t)\cdot\partial_3 G^{+,+}(\mathbf{x}_0, \mathbf{x}_0'', t)\} d\mathbf{x}_0 = 0\,. \tag{3.54}$$

Substituting equation 3.52 and 3.53 into equation 3.54 leads to

$$\partial_3 G^{-,-}(\mathbf{x}, \mathbf{x}_0'', \omega)|_{x_3=x_{3,0}} = \frac{1}{2} j\omega\rho(\mathbf{x}_0) R(\mathbf{x}_0'', \mathbf{x}_0, \omega)\,. \tag{3.55}$$

Transfering equation 3.55 to the time domain we have

$$\partial_3 G^-(\mathbf{x}, \mathbf{x}_0'', t)\big|_{x_3=x_{3,0}} = \frac{1}{2}\rho(\mathbf{x}_0)\frac{\partial R(\mathbf{x}_0'', \mathbf{x}_0, t)}{\partial t}\,. \tag{3.56}$$

$G^{-,+}(\mathbf{x}_0, \mathbf{x}_0'', t)$ is no longer directly equivalent to $R(\mathbf{x}_0'', \mathbf{x}_0, t)$ (Figure 3.3) like we discussed in Section 3.2.3. This is because the change of the assumption from flux-normalized to pressure-normalized source. From equation 3.56 we can tell that theoretically the sought reflection response is the first derivative of the wave field respect to the vertical direction. In order to obtain such a reflection response we need to use a dipole source.

3.3.1.2 Flat Spectrum Wavelet

The wavelet used to generate the direct wave is the regular Ricker wavelet (Figure 3.7a), while generating the reflection response needs not only the dipole source but also a unique wavelet (Figure 3.7b). While solving the Marchenko equation we need to repeatedly convolve the reflection response with the direct wave in each iteration. We do not do wavelet deconvolution, which means that we need to eliminate the effect of convolving the wavelet contained in the reflection response many times. To solve this problem, we use a flat spectrum wavelet defined in frequency domain (the blue line in Figure 3.7c) to generate the reflection response. The flat wavelet has a constant amplitude of one over the range of the frequencies contained in Ricker wavelet. We do this in the frequency domain using the command **filtspec** from the CREWES software project. Command **filtspec** provides a bandpass filter in frequency domain and returns a frequency spectrum of the filtered data, which is the desired flat wavelet (the blue curve in Figure 3.7c). The reason that we use such a flat wavelet can be explained in both the frequency and time domain. The property of the amplitude spectrum of the wavelet being equal to one for all frequencies makes sure the frequency content of the Ricker wavelet does not change during the multiplication of the wavelets in frequency domain. Figure 3.7d further explains this in the time domain, showing that the shape of the Ricker wavelet (the orange line) does not change after convolving with the flat wavelet (the purple line). Notice that the convolved wavelet is normalized in Figure 3.7d to keep the amplitude also identical with that of the Ricker wavelet.

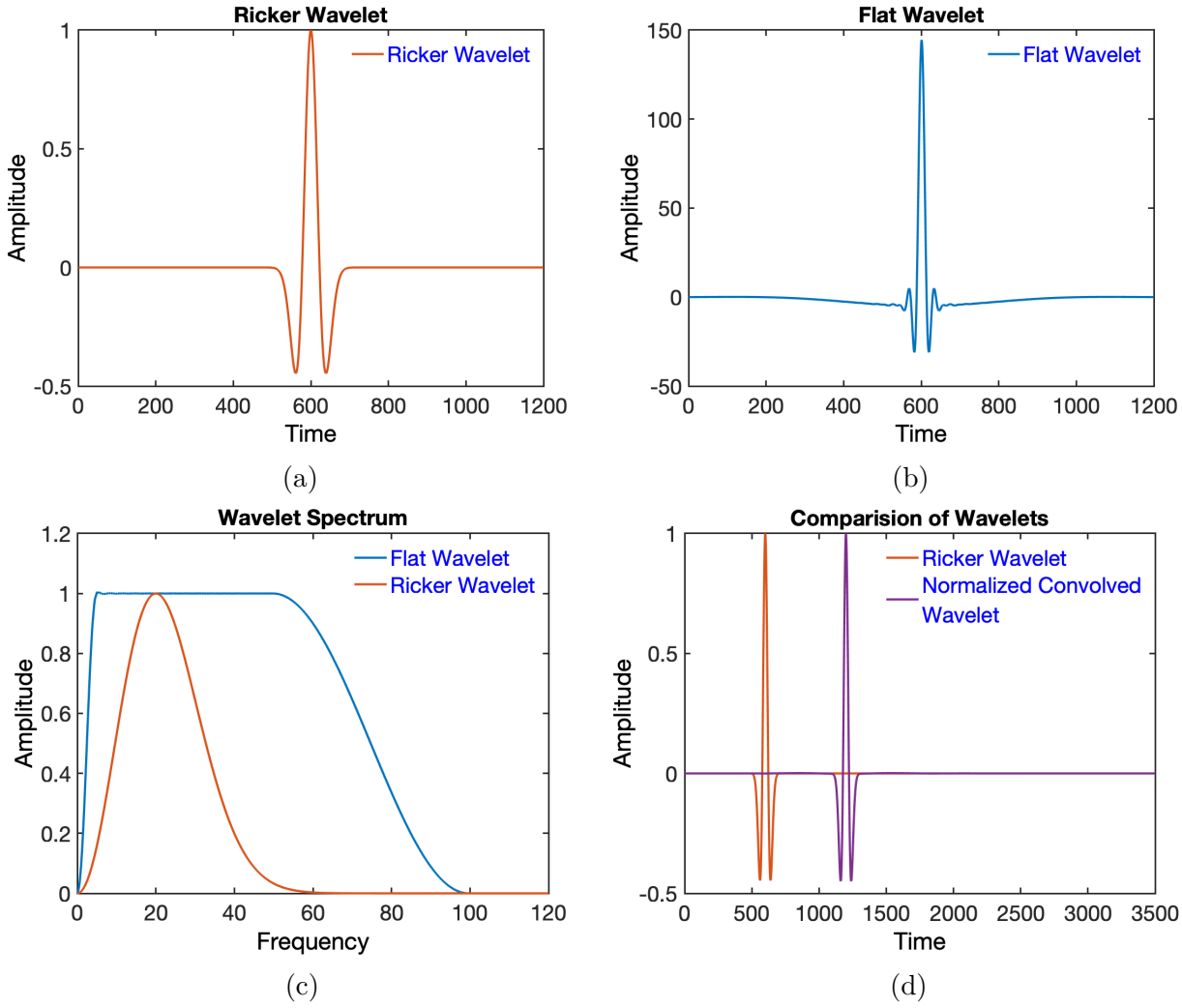

Figure 3.7: (a) Ricker wavelet in the time domain. (b) Flat wavelet in the time domain. (c) Ricker wavelet and flat wavelet in the frequency domain. (d) Ricker wavelet and normalized wavelet formed from the convolution of the Ricker and flat wavelets.

Normalization is the key to keeping the Marchenko process converging. The normalization scalar is chosen by calculating the maximum value of the convolution of the Ricker wavelet and the flat wavelet. The command in Matlab is written as $Normalization\,scalar = max(conv(Ricker\,wavlet, Flat\,wavelet))$. In my situation, the scaling value is 1994.5. Dividing the reflection response by this scalar makes sure the amplitude of the convolved data does not change within every iteration. The reflection response used in the Marchenko scheme is calculated by the finite difference modelling. We use 131 receivers and 131 dipole sources on the acquisition level to generate the 2D seismic data. Here we show the velocity model for

the simulation with only one dipole source in the middle (Figure 3.8a) and its corresponding reflection response (Figure 3.8b). Figure 3.8b is generated with a dipole source in the middle of the acquisition level with the flat wavelet. We remove the time delay caused by the flat wavelet. Moreover, the whole reflection response is divided by the scalar which we calculated above to keep the later iteration convergent.

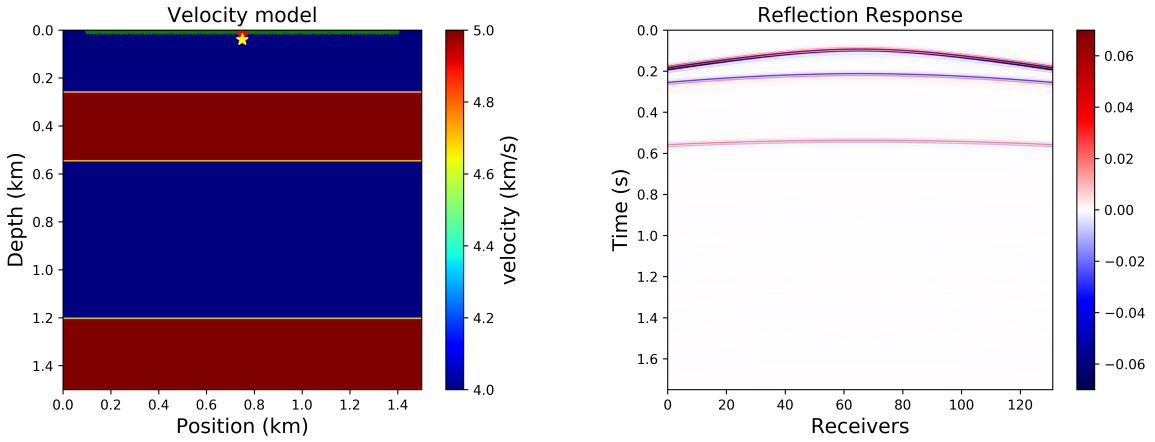

(a) (b)

Figure 3.8: (a) Velocity model. (b) Reflection response generated by the dipole source and flat wavelet and scaled by the maximum value of the convolved wavelet.

3.3.2 Direct Wave and Window Filter

Another input for the Marchenko scheme is the direct wave. As we mentioned at the end of the Section 3.2.4, the direct arrival (Figure 3.10c) is simulated by firing a virtual source (the yellow cross symbol in Figure 3.10a) inside the media and recording by the receivers (green triangles in Figure 3.10a) on the acquisition surface, using the finite difference method. While predicting the direct arrival, a smoothed velocity model (Figure 3.10a), which is calculated based on the true velocity model (Figure 3.8a) using command **velsmooth** in CREWES software project, is sufficient for the simulation. Command **velsmooth** smooths the true velocity model by convolving it with a 2D Gaussian.

Alternatively, to save calculation time, an Eikonal solver can be used to generate the direct arrival. Given the same smoothed velocity model (Figure3.10a), the solution of the Eikonal

equation gives the travel time from a specific source to each point inside this model. Using the command **eikonal2D** in the CREWES software project gives the solution of the Eikonal equation. Figure 3.10b is the travel time matrix when the source is in the middle of the acquisition surface. In order to obtain the approximate direct wave, we first need to calculate the travel time from the 131 sources on the surface to the focusing point inside the medium. Then the Ricker wavelet is convolved with the travel time, leading to the approximate direct wave (Figure3.10d). As to the computation cost, the Eikonal Equation method speeds up this part of the calculation by about 7 times compared to the finite-difference method in this example.

In Section 3.1 when the 1D Marchenko equation is iteratively solved, we use a window function to remove everything coming back after the focusing time (equation 3.5). The 3D Marchenko equation (equation 3.48) also requires that the time be smaller than the direct arrival time. Thus, to solve the 3D Marchenko equation, we need a window filter (Figure 3.10e). This window matrix removes all the events coming after the direct wave. Also this window is designed to be symmetric in time to remove all the events arriving before the time-reversed direct wave. At this point, the inputs of iteratively solving 3D Marchenko equation are all prepared.

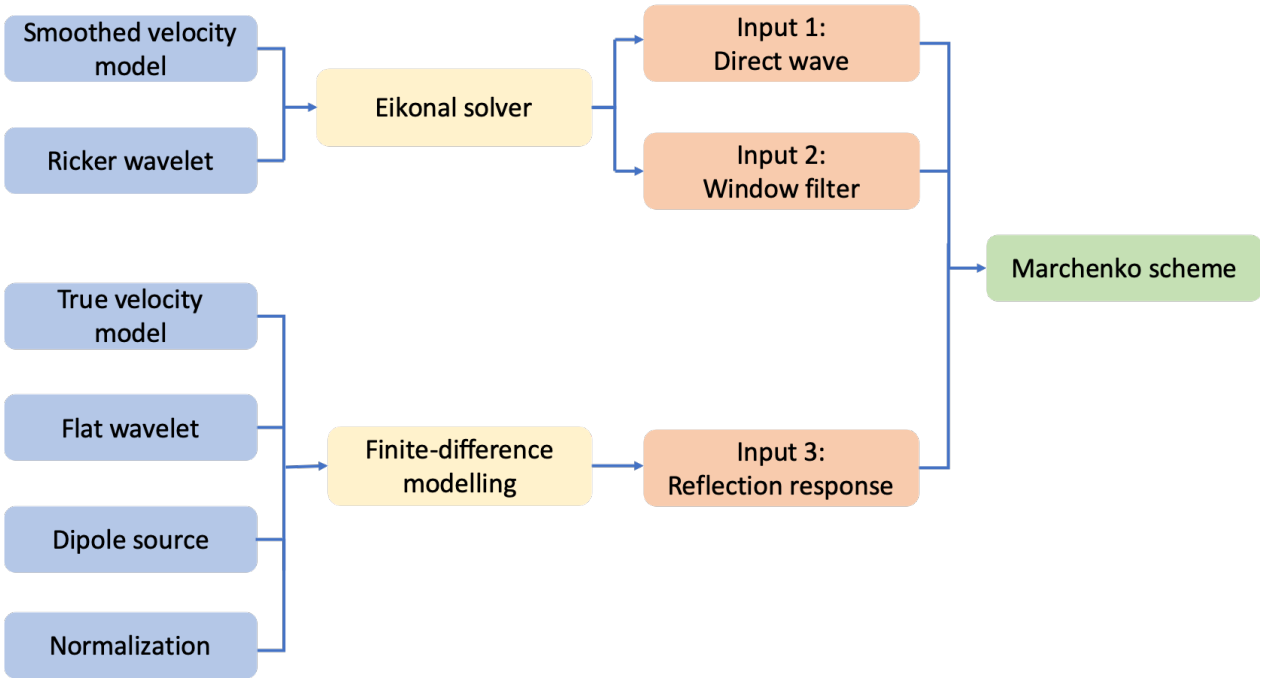

Figure 3.9: The workflow for preparing the inputs of the Marchenko scheme.

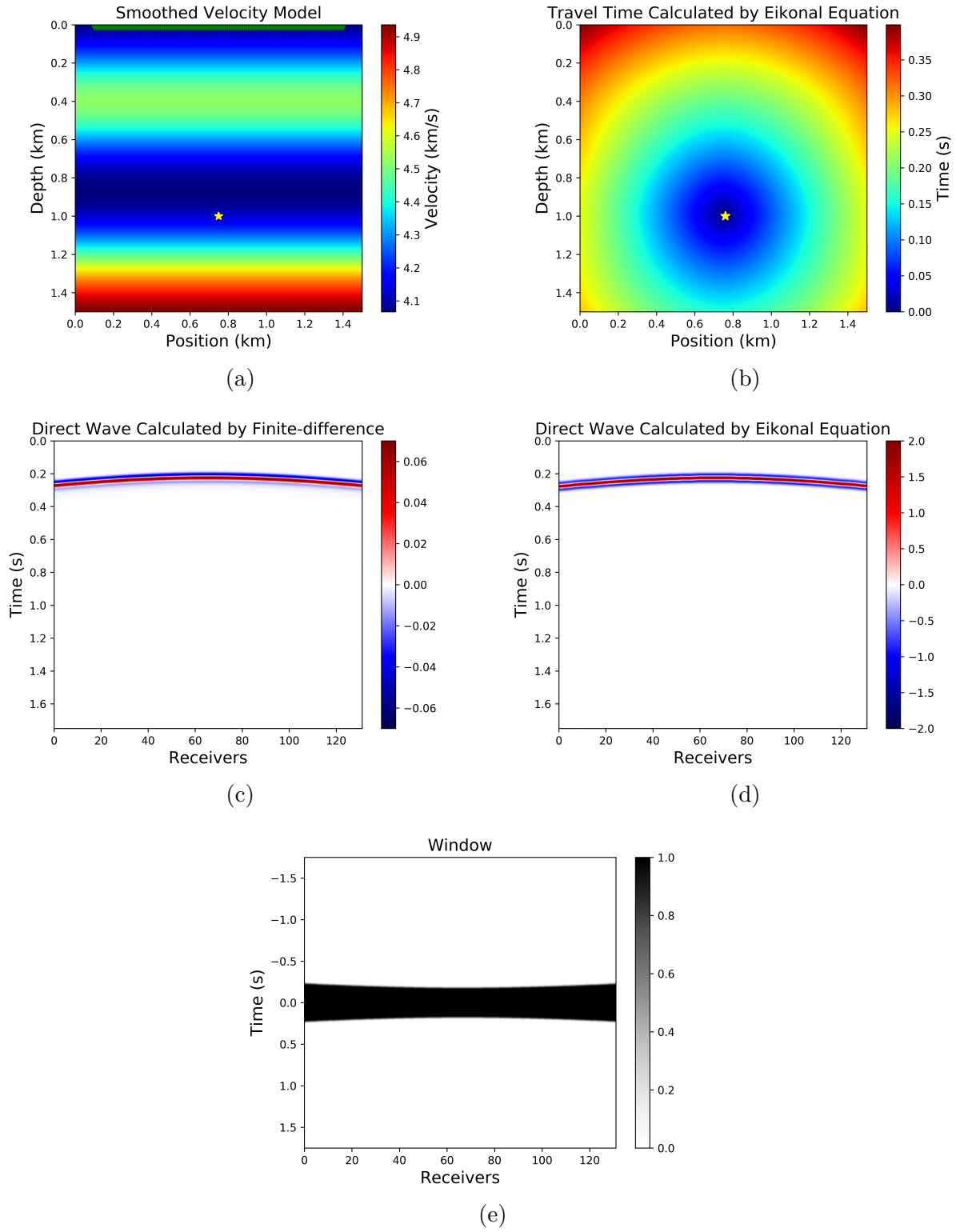

Figure 3.10: (a) Smoothed velocity model for generating the direct arrival. (b) Travel time matrix calculated with the Eikonal equation when the source is in the middle of the $z = 0$ surface. (c) Direct arrival calculated by the Finite-difference method. (d) Direct arrival calculated with Eikonal solver. (e) Window filter used to remove the waves arriving after direct wave.

3.3.3 Iteratively Retrieving Green's Function

Instead of directly solving the 3D Marchenko equation 3.48 to get the focusing functions and calculate Green's functions using equation 3.37 and 3.38, van der Neut et al. (2015) derive the coupled Marchenko equations to iteratively retrieve Green's functions, which is the standard methodology used in Marchenko Redatuming nowadays. We are going to illustrate this iteration scheme and show my simulation results.

First, I repeat the equation 3.37 and recall the definition of the forward and inverse Fourier transform as below:

$$\int_{\partial\mathbb{D}_0} f_1^+(\mathbf{x}_0, \mathbf{x}_i', \omega) R(\mathbf{x}_0'', \mathbf{x}_0, \omega) d\mathbf{x}_0 - f_1^-(\mathbf{x}_0'', \mathbf{x}_i', \omega) = G^{-,+}(\mathbf{x}_i', \mathbf{x}_0'', \omega)\,. \tag{3.57}$$

$$p(\omega) = \int_{-\infty}^{+\infty} \mathrm{d}t \exp(-j\omega t) p(t)\,. \tag{3.58}$$

$$p(t) = \frac{1}{2\pi} \int_{-\infty}^{+\infty} \mathrm{d}\omega \exp(j\omega t) p(\omega)\,. \tag{3.59}$$

Substituting equation 3.59 for f_1^+ in equation 3.57 and slightly changing the sequence of the terms in the equation leads to

$$f_1^-(\mathbf{x}_0'', \mathbf{x}_i', \omega) + G^{-,+}(\mathbf{x}_i', \mathbf{x}_0'', \omega) = \int_{\partial\mathbb{D}_0} d\mathbf{x}_0 R\left(\mathbf{x}_0'', \mathbf{x}_0, \omega\right) \times \int_{-\infty}^{+\infty} \mathrm{d}\tau \exp(-j\omega\tau) f_1^+\left(\mathbf{x}_0, \mathbf{x}_i', \tau\right)\,. \tag{3.60}$$

Taking the inverse Fourier transform of both side of equation 3.60, the result gives

$$\begin{aligned} & f_1^-\left(\mathbf{x}_0'', \mathbf{x}_i', t\right) + G^{-,+}\left(\mathbf{x}_i', \mathbf{x}_0'', t\right) \\ & = \left[\frac{1}{2\pi} \int_{-\infty}^{+\infty} \mathrm{d}\omega \exp(j\omega t) \int_{\partial\mathbb{D}_0} d\mathbf{x}_0 R\left(\mathbf{x}_0'', \mathbf{x}_0, \omega\right) \times \int_{-\infty}^{+\infty} \mathrm{d}\tau \exp(-j\omega\tau)\right] f_1^+\left(\mathbf{x}_0, \mathbf{x}_i', \tau\right) \end{aligned}\,. \tag{3.61}$$

We define the term inside the brackets as operator $\mathbf{R}$, combining the Fourier transformation, multidimensional convolution with the reflection response and the inverse Fourier transform.

Further we simplify the notation in equation 3.61 as

$$\mathbf{G}^{-} = \mathbf{R}\mathbf{f}_1^{+} - \mathbf{f}_1^{-} \,. \tag{3.62}$$

Similarly, we rewrite equation 3.38 as

$$\mathbf{G}^{+*} = \mathbf{f}_1^{+} - \mathbf{R}^{*}\mathbf{f}_1^{-} \,. \tag{3.63}$$

As mentioned in Section 3.1, the key to the autofocusing scheme is the window function. In 3D case, a window function is introduced as well. van der Neut et al. (2015) define a window matrix $\mathbf{\Theta}$ to remove all the events coming after the direct arrival, including the direct wave itself. This window filter is also set to be symmetric in time to remove the events coming before the time-reserved direct wave. Thus, because of causality, all the events in the Green's function are removed after the window filter is applied to it. We have relations between window function and Green's functions as

$$\mathbf{\Theta}\mathbf{G}^{-} = \mathbf{0} \,. \tag{3.64}$$

$$\mathbf{\Theta}\mathbf{G}^{+*} = \mathbf{0} \,. \tag{3.65}$$

The focusing functions f_2^{-}, f_1^{+} and the transmission response T are related by equations 3.46 and 3.30. Following the same derivation process which is used to derive equation 3.62, we have

$$\delta = \mathbf{T}\mathbf{f}_1^{+} \,. \tag{3.66}$$

The transmission response, T contains the direct arrival and the coda caused by the down-going internal multiple reflections, expressed as

$$\mathbf{T} = \mathbf{T}_d + \mathbf{T}_m \,. \tag{3.67}$$

A focusing function for the direct wave, $\mathbf{f}_{1d}^{+}$, is defined, via

$$\delta = \mathbf{T}_d \mathbf{f}_{1d}^{+} \,. \tag{3.68}$$

The rest of the focusing function $\mathbf{f}_1^{+}$ is defined as $\mathbf{f}_{1m}^{+}$ and

$$\mathbf{f}_1^{+} = \mathbf{f}_{1d}^{+} + \mathbf{f}_{1m}^{+} \,. \tag{3.69}$$

Substituting equation 3.69, 3.67 into 3.66 leads to

$$\mathbf{T}_m \mathbf{f}_{1d}^{+} = -\mathbf{T}_d \mathbf{f}_{1m}^{+} - \mathbf{T}_m \mathbf{f}_{1m}^{+} \,. \tag{3.70}$$

The earliest events on the right hand of the equation 3.70 comes from the convolution of the direct wave $\mathbf{T}_d$ with the first event in $\mathbf{f}_{1m}^{+}$. Considering causality, the first event of the left hand of the equation 3.70, $\mathbf{T}_m \mathbf{f}_{1d}^{+}$, should arrive at the same time with $\mathbf{T}_d \mathbf{f}_{1m}^{+}$. As $\mathbf{T}_d$ comes earlier than $\mathbf{T}_m$, $\mathbf{f}_{1m}^{+}$ cannot contain any events coming earlier than $\mathbf{f}_{1d}^{+}$, which is the time-reversed direct wave. Applying the window filter to $\mathbf{f}_1^{+}$ results

$$\mathbf{\Theta} \mathbf{f}_1^{+} = \mathbf{\Theta} \left(\mathbf{f}_{1d}^{+} + \mathbf{f}_{1m}^{+} \right) = \mathbf{f}_{1m}^{+} \,. \tag{3.71}$$

Based on the similar causality analysis, the relation between window and $\mathbf{f}_1^{-}$ is

$$\mathbf{\Theta} \mathbf{f}_1^{-} = \mathbf{f}_1^{-} \,. \tag{3.72}$$

Bringing the relation of the focusing functions and the Green's functions with the window filter into equation 3.62 and 3.63 leads to the coupled Marchenko equations

$$\mathbf{f}_1^{-} = \mathbf{\Theta} \mathbf{R} \mathbf{f}_{1d}^{+} + \mathbf{\Theta} \mathbf{R} \mathbf{f}_{1m}^{+} = \mathbf{\Theta} \mathbf{R} \mathbf{f}_1^{+} \,. \tag{3.73}$$

$$\mathbf{f}_{1m}^{+} = \boldsymbol{\Theta}\mathbf{R}^{\star}\mathbf{f}_{1}^{-} \,. \tag{3.74}$$

The window matrix $\boldsymbol{\Theta}$, reflection response $\mathbf{R}$ and direct arrival $\mathbf{T}_d$ are correctly setup in Section 3.3.1 and 3.3.2.

Now we are going to go through how to iteratively generate the Green's functions (workflow 3.11).

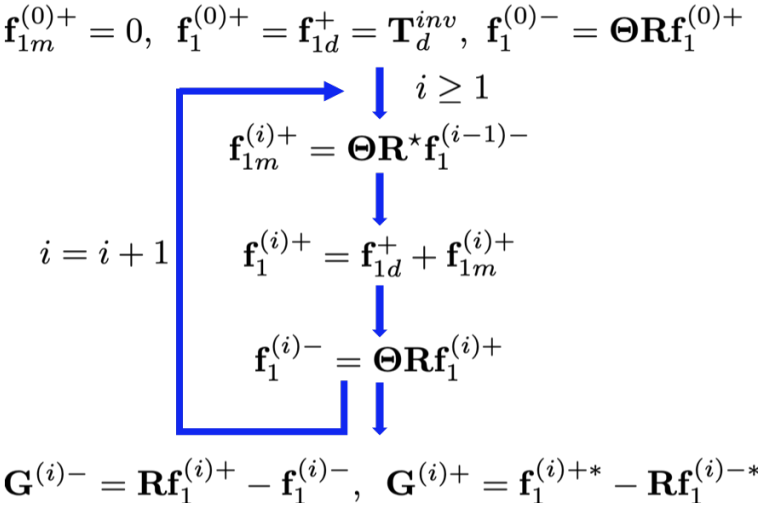

Figure 3.11: The workflow for iteratively solving the 3D Marchenko equation for the Green's functions.

The initial value of $\mathbf{f}_1^+$ (Figure 3.12a) is

$$\mathbf{f}_{1}^{(0)+} = \mathbf{f}_{1d}^{+} = \mathbf{T}_{d}^{inv}, \quad \mathbf{f}_{1m}^{(0)+} = 0 \,. \tag{3.75}$$

Based on equation 3.73, $\mathbf{f}_1^{(0)-}$ is updated by multiplying the window function and doing a multidimensional convolution of the reflection response with $\mathbf{f}_1^{(0)+}$ (Figure 3.12b). Subsquently, $\mathbf{f}_{1m}^{(1)+}$ is updated via equation 3.74 from which we can further update $\mathbf{f}_1^{(1)+}$ via equation 3.69 (Figure 3.12c). The up- and down- going Green's functions can be calculated with equation 3.62 and 3.63 (Figure 3.12e and 3.12f). Figure 3.12g is the total Green's function after ten iterations. Figure 3.12h is the shot gather calculated via finite-difference based on the velocity model given in Figure 3.12i,where the source is at the focusing point and the receivers are on the surface. Comparing Figure 3.12g and 3.12h leads us to conclude that iteratively

solving the coupled Marchenko equation retrieves the Green's function as if the source is in the subsurface.

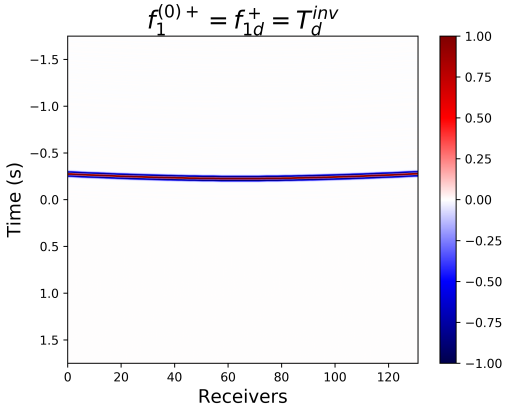

(a)

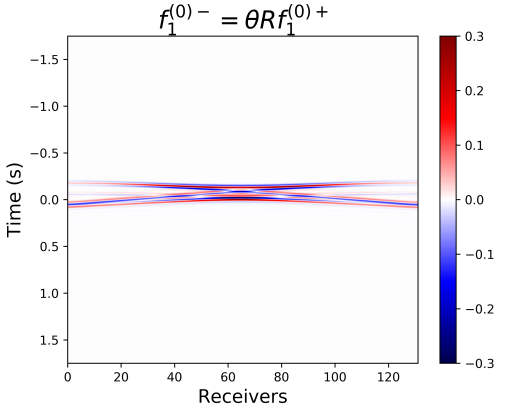

(b)

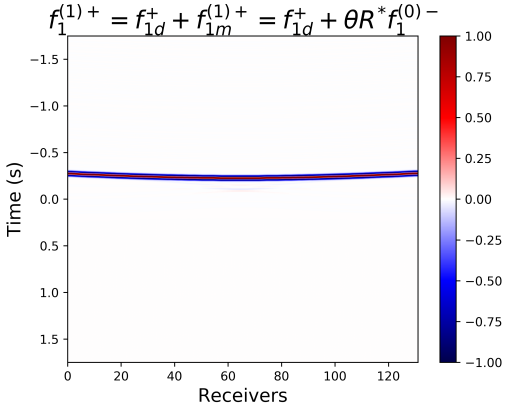

(c)

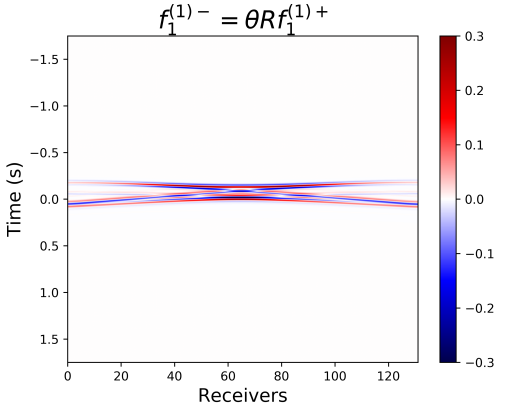

(d)

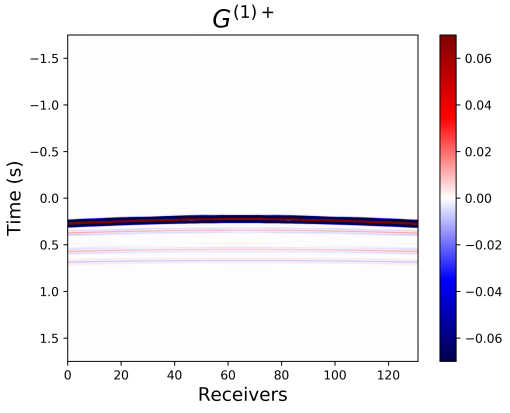

(e)

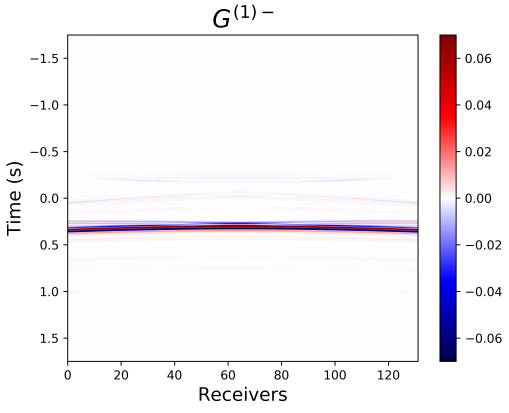

(f)

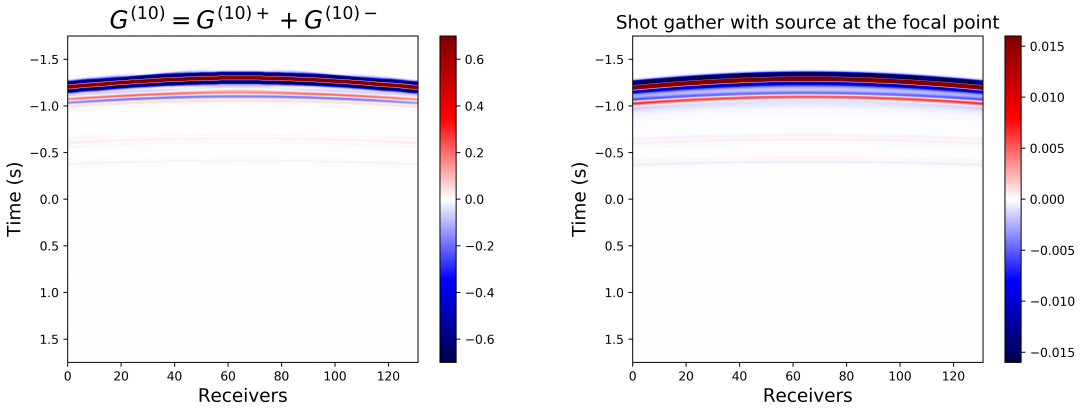

(g)

(h)

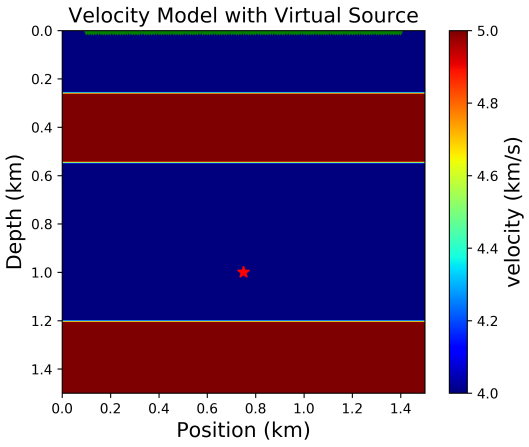

(i)

Figure 3.12: (a) Initial focusing function $\mathbf{f}_{10}^{+}$ (via equation 3.75). (b) Initial focusing function $\mathbf{f}_{10}^{-}$ (via equation 3.73). (c) Focusing function $\mathbf{f}_{11}^{+}$ after one iteration (via equation 3.74 and 3.69). (d) Focusing function $\mathbf{f}_{11}^{-}$ after one iteration (via equation 3.73). (e) Green's function $\mathbf{G}_{1}^{+}$ after one iteration (via equation 3.63). (f) Green's function $\mathbf{G}_{1}^{-}$ after one iteration (via equation 3.62). (g) Green's function $\mathbf{G}$ after ten iterations. (h) The shot gather calculated by finite-difference with a source at the focusing point and receivers on the surface (the ground truth). (i) The velocity model for shot gather in (h).

Chapter 4

Diffraction Imaging based on Marchenko Redatuming

In this chapter, we will go through the whole process of imaging the point scatterer using the Marchenko redatuming. Marchenko redatuming consists of two steps, starting from the sources and the receivers both located at the acquisition surface. The first step is Green's functions retrieval based on the Marchenko equation, allowing us to redatum the receivers from the surface to the subsurface. The second step is seismic interferometry redatuming, allowing us to redatum the sources from the surface to the subsurface. After conducting these two steps the data, which are virtually excited and recorded from the virtual sources and virtual receivers in the subsurface are generated. Using these data as the input of the RTM procedure will give us better diffraction imaging results.

Concretely, we first generate the two inputs of the Marchenko scheme, the reflection response and direct wave, and then iteratively retrieve the Green's function. Subsequently we do the interferometric redatuming using the retrieved Green's functions. In the end, we filter the redatumed data and conduct the RTM.

4.1 Reflection Response Generated from the Surface Sources and Receivers

In this section, we start from the normal acquisition system shown in Figure 4.1a. The 151 surface receivers, denoted as the green triangles, and the 151 dipole sources, denoted as the red and yellow stars, are located near the surface. The velocity model with extent 1.5 km by 1.5 km contains three layers and one point scatterer indicated as the right dot at depth 1.0 km. The wavelet used to generate the shot gather is the flat spectrum wavelet, introduced in Section 3.3.1.2. We get a 3D shot gather dataset with the size of $N_{time\ samples} \times N_{surface\ receivers} \times N_{surface\ sources}$ (here $2201 \times 151 \times 151$). The simulated shot gather shown in Figure 4.1b is excited from the middle dipole sources laterally located at 0.75 km. Now one of the inputs of the Marchenko procedure, the reflection response, is prepared.

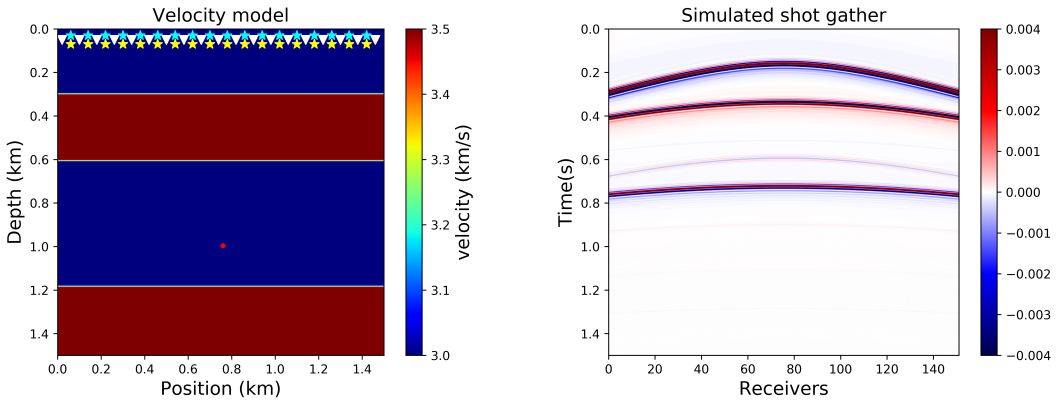

(a) (b)

Figure 4.1: (a) The velocity model with three layers and one point scatterer. The receivers (green triangles) and the dipole sources (red and yellow stars) are located on the surface. (b) The simulated shot gather generated by dipole sources and flat wavelet based on model 4.1a.

4.2 Direct Wave Generated from Virtual Source

In order to do the Marchenko Green's function retrieval, in addition to the reflection response obtained from the sources and receivers in the near surface, we also need a direct

wave shot gather. This direct wave is the initial value of the focusing function f_1^+ and can be easily obtained from the smoothed velocity model and a desired virtual source location, which is decided by the researcher. The direct wave is generated by convolving the Ricker wavelet with the travel time, which we calculate using an Eikonal solver. Figure 4.2b shows the travel time from the one virtual source to the surface receivers. Convolving with the Ricker wavelet, we get the direct wave shot gather shown in Figure 4.2c.

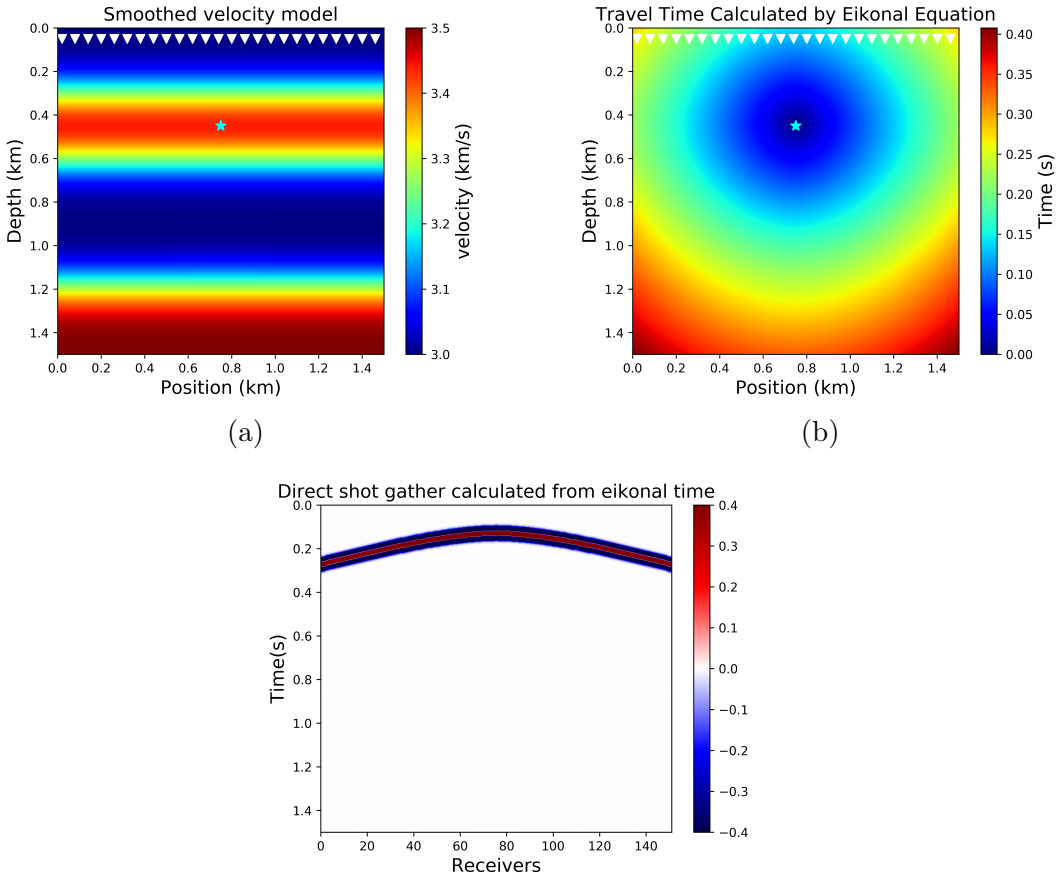

Figure 4.2: (a) The smoothed velocity model with virtual source and surface receivers. (b) The travel time from the virtual source calculated by Eikonal solver. (c) The direct wave generated from the Eikonal travel time and Ricker wavelet.

4.3 Green's Function Retrieved by Marchenko Equation

With the two prepared inputs obtained in Section 4.1 and 4.2, following the iterative solving procedure we describe in Section 3.3.3, we get the retrieved Green's function shown in Figure 4.3b. This can be regarded as the Green's function excited from the subsurface source (the blue star in model 4.3a) and recorded by the surface receivers (the green triangles in model 4.3a) in the real velocity model.

Given location information of a set of desired virtual sources (i.e. the blue stars in Figure 4.3c), we compute a 3D Green's function gather with the size of $N_{time\ samples} \times N_{surface\ receivers} \times N_{virtual\ sources}$ (here $2201 \times 151 \times 101$). Based on the reciprocity theory, the location of the surface receivers and the virtual sources can be exchanged, which leads to the model shown in Figure 4.3d. So far, using Marchenko Green's function retrieval, we have already redatum all the surface receivers to the subsurface.

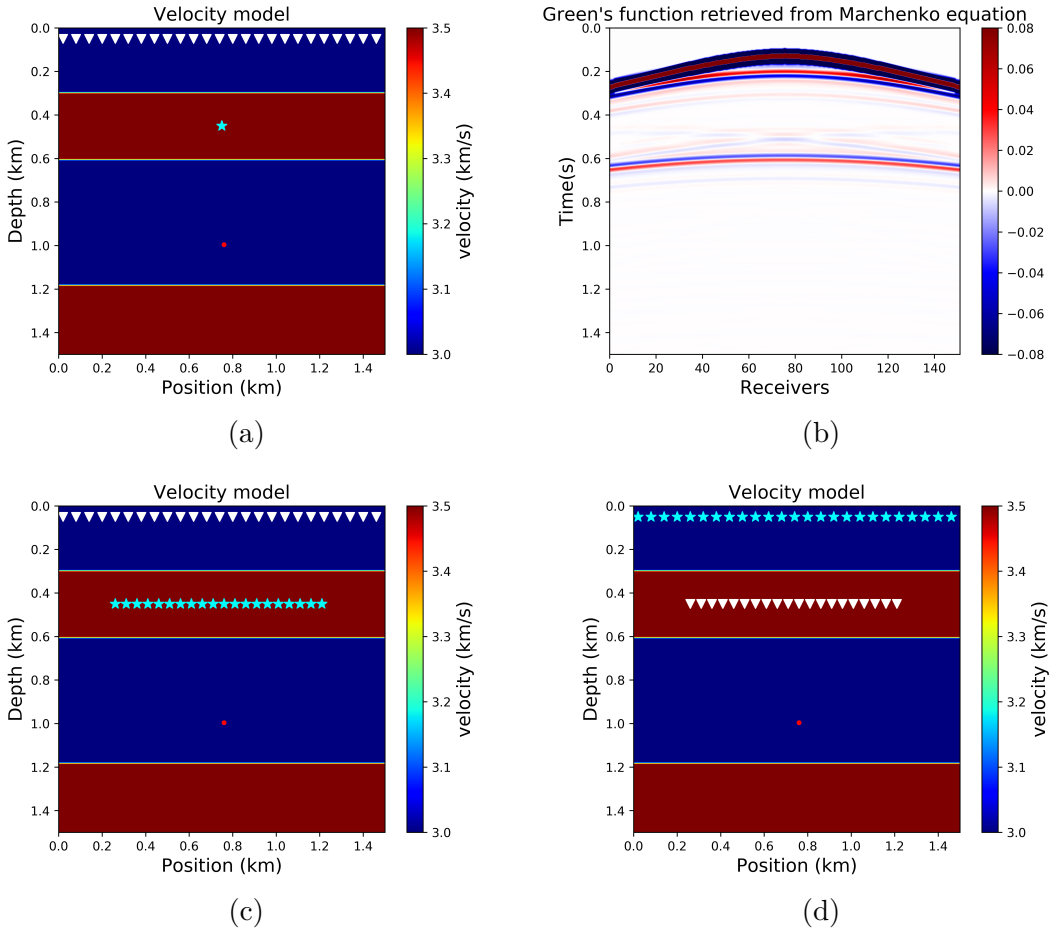

Figure 4.3: (a) The velocity model with one virtual source (blue star) in the subsurface and a line of receivers (green triangles) on the surface. (b) The Green's function retrieved from the Marchenko equation, as if it is excited by the virtual source and recorded by the surface receivers in model 4.3a. (c) The velocity model with a number of virtual sources in the subsurface. (d) The velocity model with the geometry using the reciprocity theory to exchange the position of the sources and the receivers.

4.4 Interferometry Redatuming

Seismic interferometry is a method to create virtual sources at the position of the receivers. Traditionally, if creating a virtual source in the subsurface, the receivers need to be placed in the subsurface (usually in wells). However, using the Marchenko method, there is no need for the receivers to be placed at the position of the virtual source. We can use the Marchenko Green's function retrieval method discussed in Section 4.3 to numerically redatum the surface

receivers to desired positions. In this section, we are going to use the retrieved Green's function we calculated in Secion 4.3 as input to do the seismic interferometry redatuming. The aim of doing this is to get the redatumed data excited from the virtual source (yellow star in model 4.4a) and recorded by the virtual receivers (blue triangles in model 4.4a). To this end, we use the cross-correlation method. In this section, we denote a single trace excited by one virtual source by V_S and one surface source by S_S. We denote that the data from these sources and recorded at a virtual receiver, VR as $V_S V_R$ or $S_S V_R$. As shown in Figure 4.4c, cross-correlating the trace $S_{S1}V_{R1}$ with the trace $S_{S1}V_{R2}$ leads to trace $(V_{S1}V_{R2})_1$, as if V_{R1} is the new virtual source V_{S1}. Note that the trace $(V_{S1}V_{R2})_1$ does not fully represent the trace excited by the virtual source V_{S1} and recorded by the virtual receiver V_{R2}, it is only the part that contains the information contributed by the surface source S_{S1}. Considering the surface sources S_{Sn}, we have $(V_{S1}V_{R2})_n = S_{Sn}V_{R1} \otimes S_{Sn}V_{R2}$, where $\otimes$ denotes the temporal convolution. To estimate the fully reconstructed trace $V_{S1}V_{R2}$, we have:

$$V_{S1}V_{R2} = \sum_{i=1}^{n} S_{Si}V_{R1} \otimes S_{Si}V_{R2}\,, \tag{4.1}$$

where n is the number of the surface sources. For the traces that are excited at V_{S1} and recorded by each V_{Rk}, the cross-correlation and the summation need to be repeated as:

$$V_{S1}V_{Rk} = \sum_{i=1}^{n} S_{Si}V_{R1} \otimes S_{Si}V_{Rk}\,. \tag{4.2}$$

Concatenating all of these traces, we can obtain the virtual shot gather as shown in Figure 4.4b. So far, we have redatumed both the sources and the receivers to the underground.

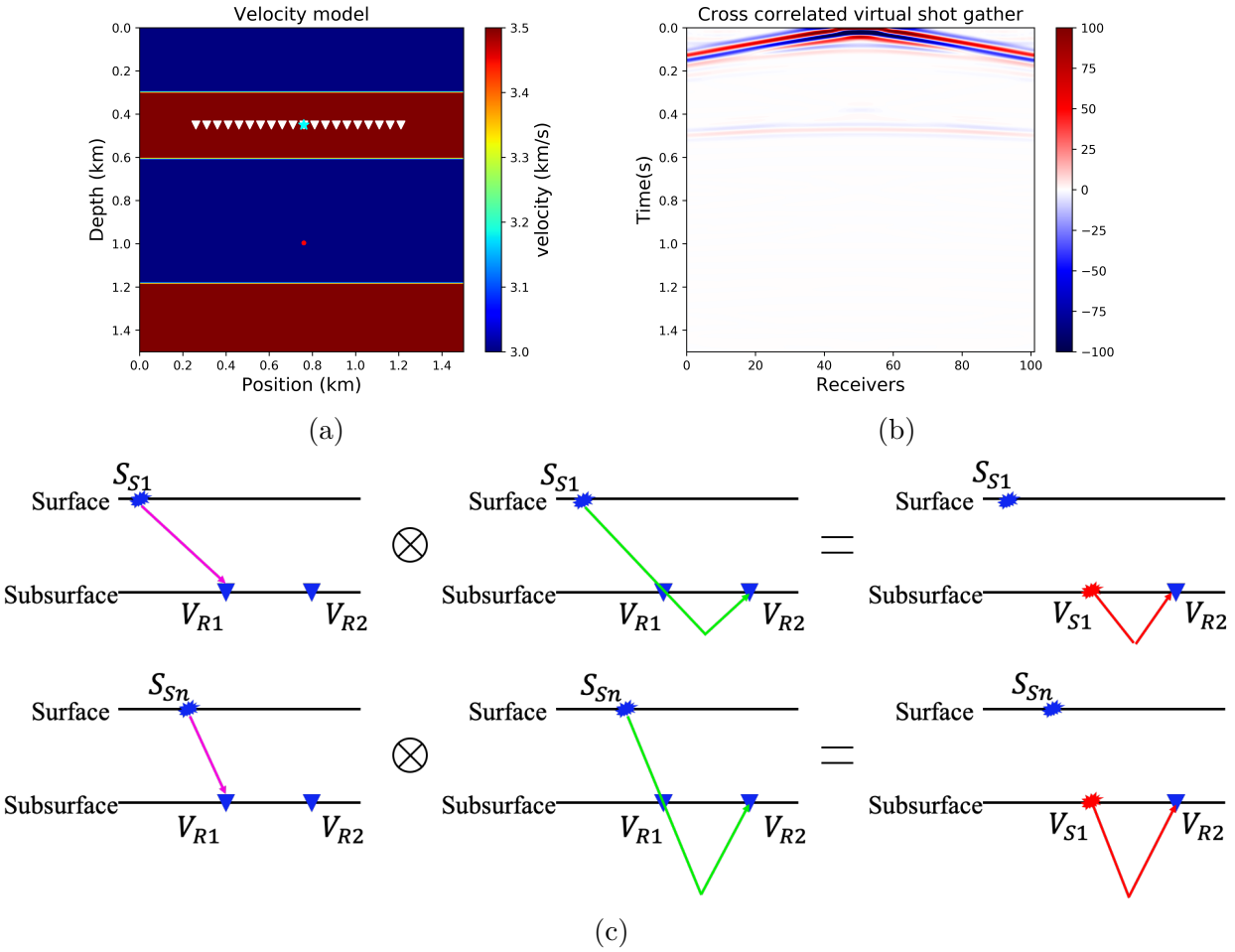

Figure 4.4: (a) The velocity model with virtual source (yellow star) and virtual receivers (blue triangles). (b) The virtual shot gather generated by cross-correlation of the Marchenko retrieved Green's functions. (c) Illustration of how the cross-correlation works.

4.5 Diffraction Imaging

Section 4.4 states that we have the ability to move the sources and the receivers to wherever we want in the subsurface. Recalling the conclusion we draw in Chapter 2, we are going to redatum the receivers in a line and a semi-circle separately in this section.

4.5.1 Virtual Receivers Placed on a Line

In Section 2.1, we tested the quality of the diffraction imaging when the receivers are placed on a line in the subsurface. We conclude that the source and the receivers should be placed on the same side of the point scatterer and near to it but not in the same layer with the point scatterer in order to avoid source artifacts. Thus we decide that the preferred virtual source and receiver position is in the second layer at depth 0.45 km (shown in Figure 4.5b). Based on the Green's function retrieved by Marchenko equation, we do the cross-correlation and successfully get the virtual source gather. But before using it to do the RTM imaging, we need to remove the direct wave. The left panel in Figure 4.5a displays the same shot gather as that shown in Figure 4.4b. We can tell that the direct wave and the reflections are overlapping and difficult to separate via travel time. Obviously, the direct wave of the virtual shot gather comes from the cross-correlation of the direct wave in each retrieved Green's function. The direct wave we generated with the Eikonal solver in Section 4.2 is thus composed from the direct wave in the Green's function. So we do the same cross-correlation procedure mentioned in Section 4.4 with the direct wave calculated in Section 4.2 and get the direct wave in the virtual shot gather, shown in the middle panel in Figure 4.5a. Notice that the amplitude of these two shot gathers are not the same, in order to do the subtraction and better visualize them, we normalize them to make the amplitude in the same range. The right panel in Figure 4.5a is the subtracted shot gather. Ideally it should only contain information from the reflections and the diffractions. However, there are still some residual of the direct wave because of the amplitude difference between the total and direct cross-correlation shot gathers. This may affect our imaging result by introducing source artifacts.

Figure 4.5c is the imaging result based on the redatumed data generated from the virtual source and the virtual receivers shown in Figure 4.5b. We can see the strong source artifact because of the residual of the direct wave on the subtracted shot gather. Meanwhile, the reflection remains strong. Although the diffracted energy can be seen focusing at the location of the point scatterer, the influence of the layer makes the distinguishing of the diffracted

energy difficult. This virtual receivers layout cannot help separate the diffractions from the reflections, so the result is not very ideal and I will illustrate this more in the discussion section.

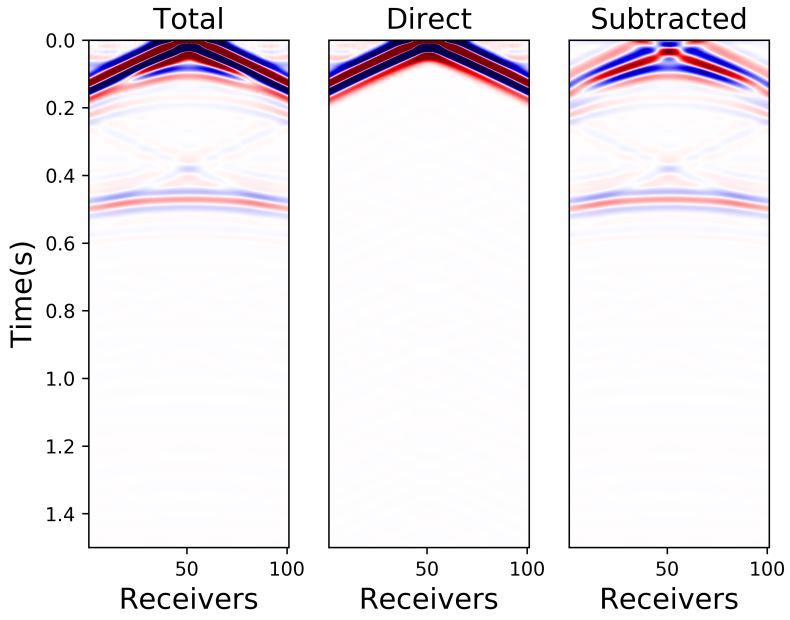

(a)

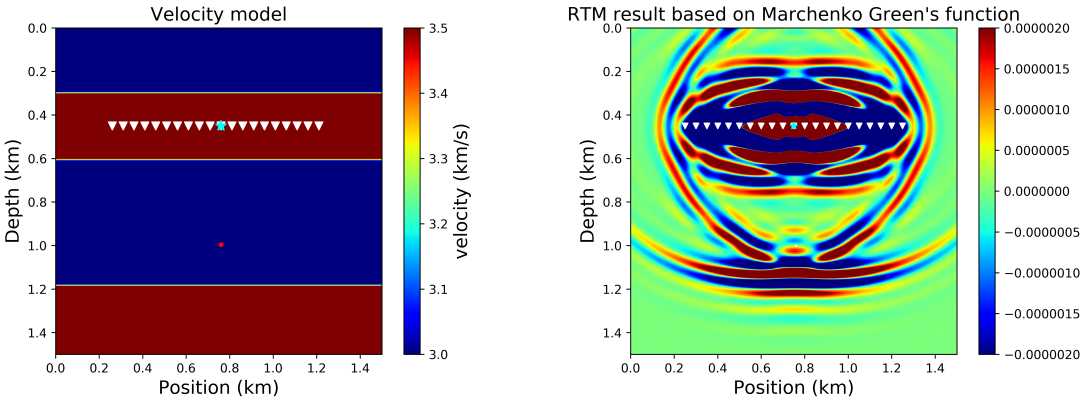

(b) (c)

Figure 4.5: (a) The total, direct and subtracted virtual shot gather by cross-correlation. (b) The velocity model with virtual source and lined virtual receivers. (c) The RTM result based on the subtracted cross-correlation shot gather in the left panel in Figure 4.5a.

4.5.2 Virtual Receivers Placed as a Semi-circle

We now investigate the other chosen geometry layout discussed in Chapter 2 which is the semi-circle virtual receiver set. In Section 2.2, we test the possibility of placing the receivers on a semi-circle by forward modelling and get a superior result. In the forward modelling, a real source is placed in the subsurface so there is no difference in putting the receivers concavely up or down. While when we redatum the source and receivers to the subsurface using cross-correlation method, the media above the sources and the receivers are regarded as homogenous. In that case, we need to put the receivers concavely down as shown in model 4.6b. Similar to all of the procedures used to redatum the line of virtual receivers, the only step we change here are the desired virtual receivers positions. Figure 4.6a shows the total, direct and the subtracted cross-correlation virtual shot gather. There is residual energy of the direct wave at the subtracted cross-correlation as well, but we can use f-k filter and the variance filter we introduced in Section 2.2 to eliminate them, so this does not affect the final imaging result. The RTM imaging is conducted after filtering the subtracted virtual shot gather, shown in Figure 4.6c. The imaging focuses the diffraction energy on the correct position and eliminates the reflection energy effectively, giving an excellent diffraction imaging result.

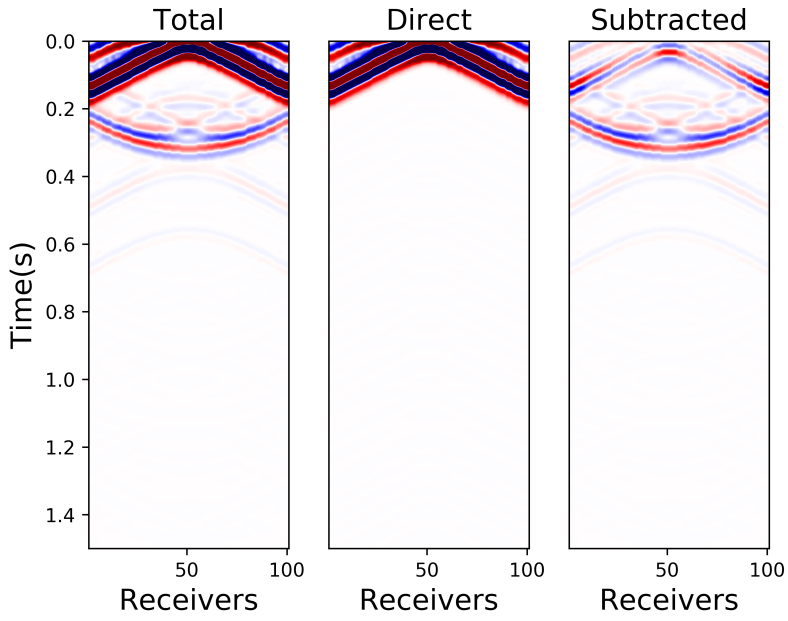

(a)

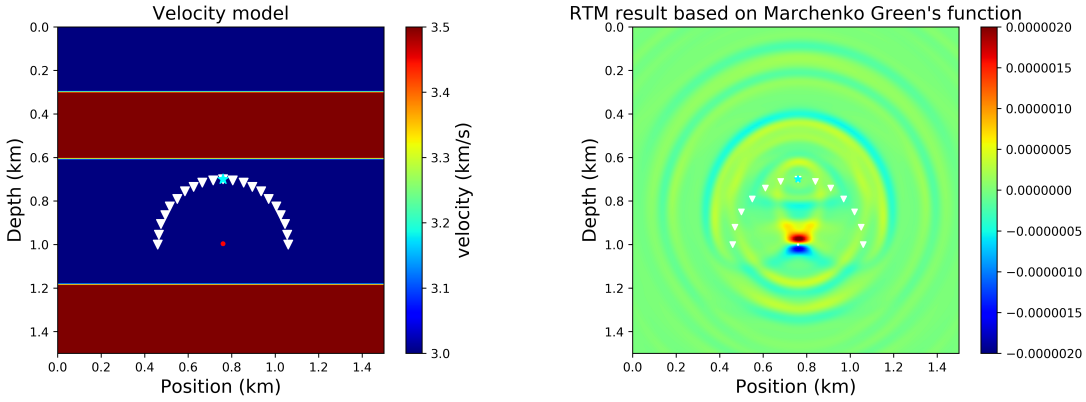

(b) (c)

Figure 4.6: (a) The total, direct and subtracted virtual shot gather by cross-correlation. (b) The velocity model with virtual source and semi-circled virtual receivers. (c) The RTM result based on the subtracted cross-correlation shot gather in the left panel in Figure 4.6a.

To conclude this chapter, we summarize all the processing in this chapter into a workflow shown in Figure 4.7. We illustrate every step by showing the geometry. Starting from the dipole sources and receivers on the surface, we do the Marchenko redatuming which consists of the Marchenko Green's function retrieval and the interferometric redatuming. The Marchenko retrieval redatums the receivers to the subsurface (virtual receivers) and seismic

interferometry redatums the source to the subsurface (virtual sources). Using the shot gather generated by the virtual sources and receivers, we do the RTM imaging. Since the RTM imaging effect based on the line of virtual receivers is not successful, we choose the semi-circle plan. The f-k filter and the variance filter are conducted to filter out the reflection energy and this finally gives an excellent diffraction image. Thanks to the Marchenko redatuming we can obtain a successful diffraction imaging from the data excited and recorded from the surface.

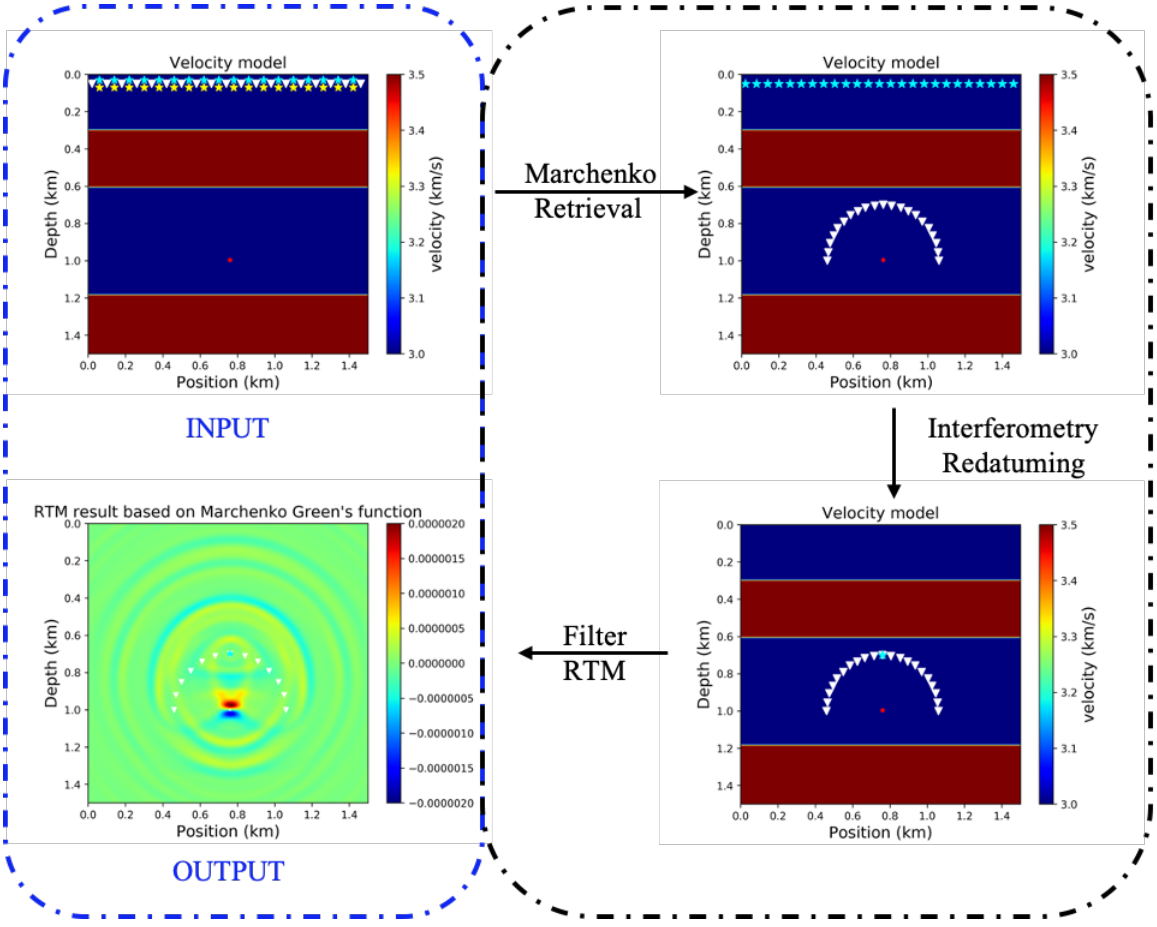

Figure 4.7: The whole procedure of doing the diffraction imaging based on Marchenko redatuming.

Chapter 5

Conclusion and Future Work

5.1 Conclusion of this Thesis

The purpose of this study is to improve diffraction imaging via Marchenko redatuming. The underlying logic is that we investigated whether placing the sources and receivers in the subsurface or changing the shape of the receiver array can enhance diffraction imaging. To this end, the Marchenko redatuming method is used to relocate the acquisition geometry.

Chapter two conducts a series of numerical modelling tests and shows that different acquisition systems do influence diffraction imaging. When the receivers are placed on a line, the sources and the receivers should be placed both below and near to the point scatterers, but not located in the same layer in order to avoid source artifacts in RTM calculations. When consider the kinematic characteristics of the diffracted wave, we innovatively propose to place the receivers on a semi-circle. The diffracted data recorded by these receivers form a straight line on the shot gather and most of the reflected data can be removed by f-k filtering. Furthermore, we filter out the signals in the shot gather which have large variance as a function of time to only keep the even and continuous events in the shot gather. This removes the artifacts caused by the edges and by reflections. The RTM imaging based on the filtered data shows only the point scatterer and the reflectors are not imaged.

Chapter three reviews the autofocusing method proposed by Rose (2001) to iteratively solve the 1D Marchenko equation. Each iteration contains four steps showing how an incident wave converges at the focusing time using the Marchenko equation. This gives a better understanding of the geophysical meaning of the Marchenko equation. Also in this chapter, we follow the derivation of the 3D Marchenko equation in Wapenaar et al. (2014). Starting from introducing the one-way reciprocity theorem and the focusing functions, we derive the relationship between the focusing functions and the Green's functions, to arrive at the 3D Marchenko equation. In this chapter we also illustrate the workflow of using the Marchenko equation to retrieve Green's functions. This includes how to generate the two inputs of the Marchenko scheme and how to iteratively solve the 3D Marchenko equation. We emphasize why we need the dipole sources and the flat wavelet to simulate the reflection response and how to use an Eikonal solver to reduce the calculation time while generating the direct wave. Chapter three gives future students a careful guide for conducting Marchenko retrieval.

Chapter four uses the Marchenko redatuming method explained in Chapter three to redatum the sources and the receivers to the favourable subsurface positions suggested in Chapter two. The results show that when the virtual receivers are located on a line, the point scatterer cannot be clearly imaged and efficiently distinguished from the reflector. However, when the virtual receivers are located on a semi-circle, after applying the f-k and variance filters to the cross-correlation shot gather, the reflections are removed and the diffractors are well imaged.

All in all, using the Marchenko redatuming method can improve the diffraction imaging. We propose two favourable source/receiver layouts. The one that the virtual receivers are located on a line does not result in very high-resolution diffraction imaging result because of the source artifacts and the influence of the reflectors. The second one, with the receivers located on a semi-circle gets very successful diffraction imaging result with the help of the F-k filter and the variance filter. In conclusion, using the Marchenko redatuming method to redatum the virtual receivers on a semi-circle around the point scatterer in the subsurface

can filter out the reflection and get an excellent diffraction imaging result.

5.2 Limitations and the Future Work

While the Marchenko equation is used to retrieve the Green's functions, the requirement on the input data are very strong. The retrieved Green's functions are sensitive to the quality of the reflection response. This is a challenge for this method.

In the present procedure, because of the residual direct wave energy in the cross-correlation shot gather, when the virtual receivers are located on a line, the diffraction imaging effect is not as good as the simulation results shown in Chapter two. The interferometry results are limited because the method we used in Chapter four is the cross-correlation based on the full wavefields. Instead of this method, the multidimensional deconvolution (MDD) Ravasi et al., 2015; Wapenaar et al., 2014 based on the decomposed Green's functions may give a more accurate redatumed result, leading to an improved diffraction imaging.

Though we get an optimized diffraction imaging result when the virtual sources are located on a semi-circle, there are challenges in using this method. This method works well partially because we know the point scatterer location, so that we can guarantee the diffraction events on the shot gather are flat. When using this method in pratical situations, we need to know the approximate location of the point scatterer. This step is not discussed in this thesis. Using the existing diffraction imaging methods can provide an approximate point scatterer location, and the method we illustrated in this thesis can be used to refine the position. Future work is expected to focus on this point.

References

Berkovitch, A., I. Belfer, Y. Hassin, and E. Landa, 2009, Diffraction imaging by multifocusing: Geophysics, **74**, WCA75–WCA81.

Brackenhoff, J., J. Thorbecke, and K. Wapenaar, 2019, Virtual sources and receivers in the real earth-considerations for practical applications: Journal of Geophysical Research: Solid Earth.

Broggini, F., and R. Snieder, 2012, Connection of scattering principles: A visual and mathematical tour: European Journal of Physics, **33**, 593.

Broggini, F., R. Snieder, and K. Wapenaar, 2011, Connection of scattering principles: Focusing the wavefield without source or receiver: Presented at the 2011 SEG Annual Meeting, Society of Exploration Geophysicists.

———, 2012, Focusing the wavefield inside an unknown 1d medium: Beyond seismic interferometry: Geophysics, **77**, A25–A28.

da Costa Filho, C. A., M. Ravasi, and A. Curtis, 2015, Elastic p-and s-wave autofocus imaging with primaries and internal multiples: Geophysics, **80**, S187–S202.

da Costa Filho, C. A., M. Ravasi, A. Curtis, and G. A. Meles, 2014, Elastodynamic green's function retrieval through single-sided marchenko inverse scattering: Physical Review E, **90**, 063201.

Hagedoorn, J. G., 1954, A process of seismic reflection interpretation: Geophysical Prospecting, **2**, 85–127.

Jia, X., A. Guitton, and R. Snieder, 2018, A practical implementation of subsalt marchenko

imaging with a gulf of mexico data set: Geophysics, **83**, S409–S419.

Kanasewich, E. R., and S. M. Phadke, 1988, Imaging discontinuities on seismic sections: Geophysics, **53**, 334–345.

Khaidukov, V., E. Landa, and T. J. Moser, 2004, Diffraction imaging by focusing-defocusing: An outlook on seismic superresolution: Geophysics, **69**, 1478–1490.

Klokov, A., and S. Fomel, 2012, Separation and imaging of seismic diffractions using migrated dip-angle gathers: Geophysics, **77**, S131–S143.

Krey, T., 1952, The significance of diffraction in the investigation of faults: Geophysics, **17**, 843–858.

Lamb, G. L., 1980, Elements of soliton theory: New York, Wiley-Interscience, 1980. 300 p.

Landa, E., and A. Maximov, 1980, Testing of algorithm for low-amplitude fault detection: Geology and Geophysics, **12**, 108–113.

Landa, E., V. Shtivelman, and B. Gelchinsky, 1987, A method for detection of diffracted waves on common-offset sections: Geophysical Prospecting, **35**, 359–373.

Liu, E., 2011, Seismic diffraction: Encyclopedia of Solid Earth Geophysics, 1097–1102.

Lomas, A., s. singh, and A. Curtis, 2019, Imaging vertical structures using marchenko methods with vertical seismic profile data: Geophysics, **85**, 1–46.

Marchenko, V. A., 1955, On reconstruction of the potential energy from phases of the scattered waves: Dokl. Akad. Nauk SSSR, 695–698.

Meles, G. A., K. Löer, M. Ravasi, A. Curtis, and C. A. da Costa Filho, 2014, Internal multiple prediction and removal using marchenko autofocusing and seismic interferometry: Geophysics, **80**, A7–A11.

Meles, G. A., K. Wapenaar, and A. Curtis, 2015, Synthesising primary reflections by marchenko redatuming and convolutional interferometry: Geophysics, **81**, Q25–Q26.

Mildner, C., F. Broggini, K. de Vos, and J. O. Robertsson, 2017a, Source wavelet amplitude spectrum estimation using marchenko focusing functions: Presented at the 79th EAGE Conference and Exhibition 2017.

———, 2019, Accurate source wavelet estimation using marchenko focusing functions: Geophysics, **84**, Q73–Q88.

Mildner, C., F. Broggini, J. O. Robertsson, D.-J. van Manen, and S. Greenhalgh, 2017b, Target-oriented velocity analysis using marchenko-redatumed data: Geophysics, **82**, R75–R86.

Moser, T., and C. Howard, 2008, Diffraction imaging in depth: Geophysical Prospecting, **56**, 627–641.

Neidell, N. S., 1997, Perceptions in seismic imaging part 2: Reflective and diffractive contributions to seismic imaging: The Leading Edge, **16**, 1121–1123.

Newton, R. G., 1982, Inverse scattering. iv. three dimensions: generalized marchenko construction with bound states, and generalized gel'fand–levitan equations: Journal of Mathematical Physics, **23**, 594–604.

Prada, C., J.-L. Thomas, and M. Fink, 1995, The iterative time reversal process: Analysis of the convergence: The Journal of the Acoustical Society of America, **97**, 62–71.

Ravasi, M., 2017, Rayleigh-marchenko redatuming for target-oriented, true-amplitude imaging: Geophysics, **82**, S439–S452.

Ravasi, M., G. Meles, A. Curtis, Z. Rawlinson, and L. Yikuo, 2015, Seismic interferometry by multidimensional deconvolution without wavefield separation: Geophysical Journal International, **202**, 1–16.

Ravasi, M., I. Vasconcelos, A. Kritski, A. Curtis, C. A. d. C. Filho, and G. A. Meles, 2016, Target-oriented marchenko imaging of a north sea field: Geophysical Supplements to the Monthly Notices of the Royal Astronomical Society, **205**, 99–104.

Rose, J. H., 2001, "single-sided" focusing of the time-dependent schrödinger equation: Physical Review A, **65**, 012707.

Singh, S., R. Snieder, J. Behura, J. van der Neut, K. Wapenaar, and E. Slob, 2015, Marchenko imaging: Imaging with primaries, internal multiples, and free-surface multiples: Geophysics, **80**, S165–S174.

Slob, E., 2016, Green's function retrieval and marchenko imaging in a dissipative acoustic medium: Physical review letters, **116**, 164301.

Snieder, R., 2015, Demystifying marchenko imaging: Presented at the 77th EAGE Conference and Exhibition-Workshops.

Sturzu, I., T. Moser, A. Popovici, N. Tanushev, I. Musat, et al., 2013, Specularity gathers for diffraction imaging: Presented at the 75th EAGE Conference & Exhibition incorporating SPE EUROPEC 2013.

Sturzu, I., A. Popovici, and T. Moser, 2014, Diffraction imaging using specularity gathers: Journal of Seismic Exploration, **23**, 1–18.

Sturzu, I., A. M. Popovici, T. J. Moser, and S. Sudhakar, 2015, Diffraction imaging in fractured carbonates and unconventional shales: Interpretation, **3**, SF69–SF79.

Taner, M. T., S. Fomel, et al., 2006, Separation and imaging of seismic diffractions using plane-wave decomposition: Presented at the 2006 SEG Annual Meeting, Society of Exploration Geophysicists.

Trorey, A., 1970, A simple theory for seismic diffractions: Geophysics, **35**, 762–784.

Tura, M. A. C., L. R. Johnson, E. L. Majer, and J. E. Peterson, 1992, Application of diffraction tomography to fracture detection: Geophysics, **57**, 245–257.

van der Neut, J., I. Vasconcelos, and K. Wapenaar, 2015, On green's function retrieval by iterative substitution of the coupled marchenko equations: Geophysical Journal International, **203**, 792–813.

Vasconcelos, I., K. Wapenaar, J. van der Neut, C. Thomson, M. Ravasi, et al., 2015, Using inverse transmission matrices for marchenko redatuming in highly complex media: Presented at the 2015 SEG Annual Meeting, Society of Exploration Geophysicists.

Wapenaar, C., and J. Grimbergen, 1996, Reciprocity theorems for one-way wavefields: Geophysical Journal International, **127**, 169–177.

Wapenaar, K., F. Broggini, E. Slob, and R. Snieder, 2013, Three-dimensional single-sided marchenko inverse scattering, data-driven focusing, green's function retrieval, and their

mutual relations: Physical Review Letters, **110**, 084301.

Wapenaar, K., J. Thorbecke, J. van der Neut, F. Broggini, E. Slob, and R. Snieder, 2014, Green's function retrieval from reflection data, in absence of a receiver at the virtual source position: The Journal of the Acoustical Society of America, **135**, 2847–2861.

Wapenaar, K., J. Thorbecke, J. van der Neut, E. Slob, F. Broggini, J. Behura, R. Snieder, et al., 2012, Integrated migration and internal multiple elimination: Presented at the 2012 SEG Annual Meeting, Society of Exploration Geophysicists.

Yilmaz, Ö., 2001, Seismic data analysis: Processing, inversion, and interpretation of seismic data: Society of exploration geophysicists.